

See discussions, stats, and author profiles for this publication at: <https://www.researchgate.net/publication/230277645>

# Theoretical HVSR curves from full wavefield modelling of ambient vibrations in a weakly dissipative layered Earth

Article in *Geophysical Journal International* · March 2010

DOI: 10.1111/j.1365-246X.2010.04560.x

CITATIONS

38

READS

123

2 authors, including:



**Dario Albarello**

Università degli Studi di Siena

185 PUBLICATIONS 2,302 CITATIONS

SEE PROFILE

Some of the authors of this publication are also working on these related projects:



PETROROV [View project](#)

# Theoretical HVSR curves from full wavefield modelling of ambient vibrations in a weakly dissipative layered Earth

Enrico Lunedei and Dario Albarello

Dipartimento di Scienze della Terra dell'Università di Siena Via Laterina 8, 53100 Siena, Italy. E-mail: albarello@unisi.it

Accepted 2010 February 9. Received 2010 January 21; in original form 2009 February 19

## SUMMARY

Ambient vibrations generated by anthropic activity in the range of frequencies of engineering interest (0.5–20 Hz) were modelled as the wavefield generated by a continuous distribution of random, independent point-like sources acting at the surface of a weakly dissipative layered Earth. A full wavefield solution was deduced analytically and used to evaluate major properties of Horizontal to Vertical Spectral Ratios (HVSR) in a representative set of selected cases of observed subsoil configurations. The results obtained confirmed—on a more coherent analytical basis—several statements deduced from empirical observations and numerical simulations, which are of great importance for practical applications. It was confirmed that HVSR cannot be considered representative of the *S*-wave response function but as concerns the possibility of detecting the presence of 1-D resonance phenomena and of identifying the resonance frequency associated with the shallowest strong impedance contrast in the subsoil. The model enables evaluations of the reliability of HVSR interpretations provided in the surface wave approximation that can be considered valid in the frequency range above the resonance frequency. At the resonance frequency, HVSR values prove sensitive to the strength of sources in the near proximity of the receiver (within a few tens of metres) and this suggests caution in the interpretation of HVSR peaks in terms of subsoil properties only.

**Key words:** Body waves; Surface waves and free oscillations; Site effects; Computational seismology; Wave propagation.

## 1 INTRODUCTION

Since the beginning of modern seismology, ambient vibrations have been the subject of experimental studies and scientific debate (e.g. Ferrari *et al.* 2000). Although such studies have been ongoing, more recently, the number of papers devoted to this topic has undergone a dramatic increase (see, e.g. Bonnefoy-Claudet *et al.* 2006a) and several international research projects have been carried out (e.g. EVG1-CT-2000-00026 SESAME, NATO-SfP980857). This renewed interest has been driven by the possibility to use such low-amplitude ground motion for cost-effective seismic characterization of subsoil and the parametrization of building dynamic response (e.g. Wenzel & Pichler 2005; Mucciarelli *et al.* 2009).

Among the available techniques, the most appealing in free-field applications is probably that made popular by Nakamura (1989), which is based on the analysis of the Horizontal to Vertical Spectral Ratios (HVSR) of ambient vibrations measured at a three-component single station. It has been shown (Bard 1999; Haghshenas *et al.* 2008) that HVSR can supply useful information about the resonance properties of the shallow subsoil and represents a cost-effective tool for microzoning studies (e.g. D'Amico *et al.* 2008).

An important aspect that has attracted much attention in recent years is the physical interpretation and modelling of the HVSR curve deduced from ambient vibrations: these are a fundamental prerequisite for establishing a link between observations and subsoil structure and thus for using ambient vibrations to infer the dynamic properties of the subsoil (Arai & Tokimatsu 2004, 2005; Parolai *et al.* 2005; Picozzi & Albarello 2007; Herak 2008). Experimental studies indicate that surface waves are ubiquitously present (e.g. Okada 2003) in ambient vibrations but provide contradictory results as regards their relative importance with respect to body waves. Theoretical models dealing with vibrations generated by individual sources (Tokimatsu 1997) and numerical simulations that consider a finite number of sources (Lachet & Bard 1994; Fäh *et al.* 2001; Bonnefoy-Claudet *et al.* 2006b, 2008) provide more straightforward indications, suggesting that the role of surface waves at frequencies higher than the resonance frequency of the local subsoil becomes increasingly important when the seismic impedance contrast at the sediment-bedrock interface increases. This inspired several authors to interpret the shape of HVSR as the effect of surface wave ellipticity only (e.g. Konno & Ohmachi 1998; Fäh *et al.* 2001; Scherbaum *et al.* 2003; Malishevsky & Scherbaum 2004). However, modelling also indicates that the contribution of Rayleigh

waves becomes less important below and at the subsoil resonance frequency (Tokimatsu 1997; Scherbaum *et al.* 2003), that is, in correspondence with the aspect of HVSR which is more interesting for practical purposes.

Despite their importance, these results cannot be considered conclusive due to the fact that the underlying models are strictly deterministic and only concern a finite number of sources located around the receiver. A more general model should account for the inherently stochastic nature of the ambient vibration wavefield (e.g. Aki 1957; Okada 2003) by providing a coherent statistical treatment of distributed sources.

A first attempt to develop a model of this kind was carried out by Arai & Tokimatsu (2004, 2005) on the assumption that surface waves dominate ambient vibrations. This model has recently been generalized by Lunedei & Albarello (2009) to include the effect of material damping in the presence of weak dissipation. However, since it is well known (e.g. Bonnefoy-Claudet *et al.* 2006a) that both body waves and surface waves contribute to ambient vibrations, the above models can be seen only as useful approximations which are justified by computational feasibility allowing their implementation in effective inversion protocols (e.g. Arai & Tokimatsu 2004; Parolai *et al.* 2005; Picozzi & Albarello 2007).

A more general model was recently provided by Tanimoto (2008), who considered a random distribution of independent, vertical point sources active at the surface of a spherical Earth. However, this model only considers the low-frequency range (well below 1 Hz) and thus cannot be applied in the case of most common applications of HVSR measurements in the field of seismic engineering and microzoning.

A new attempt in this direction is presented here. It is based on the formalization of the full wavefield generated by harmonic point sources (e.g. Harkrider 1964; Aki & Richards 1980; Hisada 1994; Ben-Menahem & Singh 2000). Unlike previous applications to ambient vibration wavefield (Bonnefoy-Claudet *et al.* 2006b, 2008), this model is generalized here to the case of a continuous distribution of random independent point sources which are active at the surface of a flat, viscoelastic layered Earth.

The relevant formalization is described in the first part of the paper along with a brief outline of the underlying computational problems and the numerical solutions adopted. The resulting model is applied to a set of subsoil configurations which are representative of possible situations encountered in the practice of ambient vibration analysis in the range of frequencies of engineering interest ([0.5, 20] Hz). The results of these computations are used to explore some features of HVSR that are important in the practice of ambient vibration analysis: the relationship existing between HVSR and the *S*-wave response function, the reliability of surface wave approximations for modelling empirical HVSR curves, the role of the near sources and the presence of a ‘skin’ effect that limits the sensitivity of HVSR to the seismic properties of deeper layers.

## 2 A PHYSICAL MODEL FOR AMBIENT VIBRATIONS

An approximate solution of the wave equation relative to far-field ground motion generated by a source can be represented in terms of surface waves (Aki & Richards 1980). More precisely, it can be expressed as a combination of the different surface waves modes, whose relative amplitudes depend on the source features. Nevertheless, it is also possible to obtain a more general solution of this

wave equation, which, for a flat, layered viscoelastic Earth, is briefly outlined below.

The Earth is modelled as a set of homogeneous, isotropic layers overlying a homogenous, isotropic half-space. The Cartesian reference frame is set with the origin on the Earth’s surface, approximated by a plane  $\mathbb{R}^2$  with horizontal coordinates  $(x, y)$  and the *z*-axis directed vertically downward: each layer *j* ( $j = 1, 2, \dots, N$ ) in the subsoil is located between the depths  $z^{j-1}$  and  $z^j$ ; index  $j = (N + 1)$  refers to the underlying half-space. Together with this Cartesian frame system  $(x, y, z)^T$ , a corresponding cylindrical system  $(r, \vartheta, z)^T$  is also used.

Let the harmonic point-like source located in  $(r, \vartheta, 0)^T$  be given as

$$\Psi e^{-i\omega t} = \begin{pmatrix} \Psi_x \\ \Psi_y \\ \Psi_z \end{pmatrix} e^{-i\omega t}, \quad (1)$$

with  $\omega \in \mathbb{R}^+$  fixed. The source components are considered in general complex, that is,  $\Psi_h \in \mathbb{C}$ ,  $h = x, y, z$ . In this frame, the general solution of the dynamic wave equation relative to the ground motion at a receiver placed at the origin is described by the relationships

$$\mathbf{u}(r, \vartheta, z; t) \equiv \begin{pmatrix} u_r(r, \vartheta) \\ u_\vartheta(r, \vartheta) \\ u_z(r, \vartheta) \end{pmatrix} e^{-i\omega t} \quad (2)$$

$$u_r(r, \vartheta) = u_r^c(r) \cos \vartheta + u_r^s(r) \sin \vartheta + u_r^n(r) \quad (3)$$

$$u_\vartheta(r, \vartheta) = u_\vartheta^c(r) \cos \vartheta + u_\vartheta^s(r) \sin \vartheta \quad (4)$$

$$u_z(r, \vartheta) = u_z^c(r) \cos \vartheta + u_z^s(r) \sin \vartheta + u_z^n(r), \quad (5)$$

with

$$u_r^c(r) \equiv - \int_0^{+\infty} \left\{ R_{1,x}(k) \frac{dJ_1(kr)}{d(kr)} + L_{1,x}(k) \frac{J_1(kr)}{kr} \right\} dk \quad (6)$$

$$u_r^s(r) \equiv - \int_0^{+\infty} \left\{ R_{1,y}(k) \frac{dJ_1(kr)}{d(kr)} + L_{1,y}(k) \frac{J_1(kr)}{kr} \right\} dk \quad (7)$$

$$u_r^n(r) \equiv - \int_0^{+\infty} R_{1,z}(k) J_1(kr) dk \quad (8)$$

$$u_\vartheta^c(r) \equiv - \int_0^{+\infty} \left\{ R_{1,y}(k) \frac{J_1(kr)}{kr} + L_{1,y}(k) \frac{dJ_1(kr)}{d(kr)} \right\} dk \quad (9)$$

$$u_\vartheta^s(r) \equiv \int_0^{+\infty} \left\{ R_{1,x}(k) \frac{J_1(kr)}{kr} + L_{1,x}(k) \frac{dJ_1(kr)}{d(kr)} \right\} dk \quad (10)$$

$$u_z^c(r) \equiv \int_0^{+\infty} R_{2,x}(k) J_1(kr) dk \quad (11)$$

$$u_z^s(r) \equiv \int_0^{+\infty} R_{2,y}(k) J_1(kr) dk \quad (12)$$

$$u_z^n(r) \equiv - \int_0^{+\infty} R_{2,z}(k) J_0(kr) dk, \quad (13)$$

where  $J_0$  and  $J_1$  are the Bessel functions of zero and first order, respectively, and the coefficients  $L$  and  $R$  are functions of  $k$  (Appendix A). These equations correspond to eq. (11) in Hisada

(1994) after the source and receiver positions are exchanged and the displacements produced by the source components are summed up. Since the coefficients  $L$  and  $R$  linearly depend on the source components (see Appendix A), one has

$$u_r(r, \vartheta) = \tilde{u}_r(r)(\Psi_x \cos \vartheta + \Psi_y \sin \vartheta) + u_r^*(r)\Psi_z \quad (14)$$

$$u_\vartheta(r, \vartheta) = \tilde{u}_\vartheta(r)(-\Psi_y \cos \vartheta + \Psi_x \sin \vartheta) \quad (15)$$

$$u_z(r, \vartheta) = \tilde{u}_z(r)(\Psi_x \cos \vartheta + \Psi_y \sin \vartheta) + u_z^*(r)\Psi_z, \quad (16)$$

with

$$\tilde{u}_r(r) = - \int_0^{+\infty} \left\{ R_{1,H}(k) \frac{dJ_1(kr)}{d(kr)} + L_H(k) \frac{J_1(kr)}{kr} \right\} dk \quad (17)$$

$$u_r^*(r) = - \int_0^{+\infty} R_{1,V}(k) J_1(kr) dk \quad (18)$$

$$\tilde{u}_\vartheta(r) = \int_0^{+\infty} \left\{ R_{1,H}(k) \frac{J_1(kr)}{kr} + L_H(k) \frac{dJ_1(kr)}{d(kr)} \right\} dk \quad (19)$$

$$\tilde{u}_z(r) = \int_0^{+\infty} R_{2,H}(k) J_1(kr) dk \quad (20)$$

$$u_z^*(r) = - \int_0^{+\infty} R_{2,V}(k) J_0(kr) dk, \quad (21)$$

where  $L_H$ ,  $R_{j,H}$  and  $R_{j,V}$  ( $j = 1, 2$ ) depend on the SH and  $P$ -SV propagator matrices (Aki & Richards 1980), as shown in Appendix A. It is worth noting that the denominators of these functions are the Love (for  $L_H$ ) and Rayleigh (for the others) secular functions (Aki & Richards 1980), having isolated singularities in correspondence with the Love and Rayleigh admissible wavenumbers  $k$ . These functions depend on the subsoil seismic structure, but not on the source configuration.

In this frame, the effect of material damping can be accounted for by considering a viscoelastic rheology for the medium (e.g. Lai & Rix 1998; Lai & Rix 2002). In this position, damping is taken into account by rendering complex the Lamé parameters, and, as a consequence, the body waves velocities. As explained in Appendix A, this only affects the coefficients  $L_H$ ,  $R_{j,H}$ ,  $R_{j,V}$  ( $j = 1, 2$ ), that is, the relative weights of the Bessel functions relative to different  $k$  values.

## 2.1 Vibrations induced by an aleatory, harmonic point load

Sources responsible for ambient vibrations are modelled as harmonic, point-like forces with stochastic amplitudes. This model (Bonnefoy-Claudet 2006b) seems to be the most suitable for representing ambient vibrations generated by anthropic sources in the range of intermediate/high frequencies (0.5–20 Hz). In this frame, the components  $\Psi_h$  ( $h = x, y, z$ ) are random variables with mean zero

$$\mathcal{M}[\Psi_x] = \mathcal{M}[\Psi_y] = \mathcal{M}[\Psi_z] = 0,$$

variances

$$\mathcal{V}[\Psi_h] = \mathcal{M}[\Psi_h^2], \quad h = x, y, z,$$

and covariances

$$\mathcal{K}(\Psi_h, \Psi_q) = \mathcal{M}[\Psi_h \cdot \overline{\Psi_q}], \quad h, q = x, y, z,$$

where the overline indicates the conjugate. Note that  $\mathcal{K}(\Psi_h, \Psi_q) = \overline{\mathcal{K}(\Psi_q, \Psi_h)}$ ,  $h, q = x, y, z$ . Linear relationships existing between ground motion and source components (14)–(16) imply a vanishing average ground motion

$$\begin{aligned} \mathcal{M}[u_r(r, \vartheta)] &= \tilde{u}_r(r)(\mathcal{M}[\Psi_x] \cos \vartheta + \mathcal{M}[\Psi_y] \sin \vartheta) \\ &\quad + u_r^*(r)\mathcal{M}[\Psi_z] = 0 \end{aligned} \quad (22)$$

$$\begin{aligned} \mathcal{M}[u_\vartheta(r, \vartheta)] &= \tilde{u}_\vartheta(r)(-\mathcal{M}[\Psi_y] \cos \vartheta + \mathcal{M}[\Psi_x] \sin \vartheta) = 0 \end{aligned} \quad (23)$$

$$\begin{aligned} \mathcal{M}[u_z(r, \vartheta)] &= \tilde{u}_z(r)(\mathcal{M}[\Psi_x] \cos \vartheta + \mathcal{M}[\Psi_y] \sin \vartheta) \\ &\quad + u_z^*(r)\mathcal{M}[\Psi_z] = 0, \end{aligned} \quad (24)$$

$\forall r, \forall \vartheta$ . The variance relative to the radial component of the ground motion becomes

$$\begin{aligned} \mathcal{V}[u_r(r, \vartheta)] &= \mathcal{M}[u_r(r, \vartheta) \cdot \overline{u_r(r, \vartheta)}] \\ &= \mathcal{V}_r(r, \vartheta) + \mathcal{K}_r(r, \vartheta), \end{aligned} \quad (25)$$

where the variance and covariance terms are

$$\begin{aligned} \mathcal{V}_r(r, \vartheta) &\equiv \mathcal{M}[u_r^c(r) \cdot \overline{u_r^c(r)}] \cos^2 \vartheta \\ &\quad + \mathcal{M}[u_r^s(r) \cdot \overline{u_r^s(r)}] \sin^2 \vartheta + \mathcal{M}[u_r^n(r) \cdot \overline{u_r^n(r)}], \end{aligned} \quad (26)$$

$$\begin{aligned} \mathcal{K}_r(r, \vartheta) &\equiv \left\{ \mathcal{M}[u_r^c(r) \cdot \overline{u_r^s(r)}] \right. \\ &\quad + \mathcal{M}[\overline{u_r^c(r)} \cdot u_r^s(r)] \left. \right\} \cos \vartheta \sin \vartheta \\ &\quad + \left\{ \mathcal{M}[u_r^c(r) \cdot \overline{u_r^n(r)}] + \mathcal{M}[\overline{u_r^c(r)} \cdot u_r^n(r)] \right\} \cos \vartheta \\ &\quad + \left\{ \mathcal{M}[u_r^s(r) \cdot \overline{u_r^n(r)}] + \mathcal{M}[\overline{u_r^s(r)} \cdot u_r^n(r)] \right\} \sin \vartheta, \end{aligned} \quad (27)$$

respectively. In the same way, the variance relative to the angular component turns out to be

$$\begin{aligned} \mathcal{V}[u_\vartheta(r, \vartheta)] &= \mathcal{M}[u_\vartheta(r, \vartheta) \cdot \overline{u_\vartheta(r, \vartheta)}] \\ &= \mathcal{V}_\vartheta(r, \vartheta) + \mathcal{K}_\vartheta(r, \vartheta), \end{aligned} \quad (28)$$

$$\begin{aligned} \mathcal{V}_\vartheta(r, \vartheta) &\equiv \mathcal{M}[u_\vartheta^c(r) \cdot \overline{u_\vartheta^c(r)}] \cos^2 \vartheta \\ &\quad + \mathcal{M}[u_\vartheta^s(r) \cdot \overline{u_\vartheta^s(r)}] \sin^2 \vartheta, \end{aligned} \quad (29)$$

$$\begin{aligned} \mathcal{K}_\vartheta(r, \vartheta) &\equiv \left\{ \mathcal{M}[u_\vartheta^c(r) \cdot \overline{u_\vartheta^s(r)}] + \mathcal{M}[\overline{u_\vartheta^c(r)} \cdot u_\vartheta^s(r)] \right\} \\ &\quad \cdot \cos \vartheta \sin \vartheta, \end{aligned} \quad (30)$$

while the vertical variance is

$$\begin{aligned} \mathcal{V}[u_z(r, \vartheta)] &= \mathcal{M}[u_z(r, \vartheta) \cdot \overline{u_z(r, \vartheta)}] \\ &= \mathcal{V}_z(r, \vartheta) + \mathcal{K}_z(r, \vartheta), \end{aligned} \quad (31)$$

$$\begin{aligned} \mathcal{V}_z(r, \vartheta) &\equiv \mathcal{M}[u_z^c(r) \cdot \overline{u_z^c(r)}] \cos^2 \vartheta \\ &\quad + \mathcal{M}[u_z^s(r) \cdot \overline{u_z^s(r)}] \sin^2 \vartheta + \mathcal{M}[u_z^n(r) \cdot \overline{u_z^n(r)}], \end{aligned} \quad (32)$$

$$\begin{aligned} \mathcal{K}_z(r, \vartheta) &\equiv \left\{ \mathcal{M}[u_z^c(r) \cdot \overline{u_z^s(r)}] \right. \\ &\quad + \mathcal{M}[\overline{u_z^c(r)} \cdot u_z^s(r)] \left. \right\} \cdot \cos \vartheta \sin \vartheta \\ &\quad + \left\{ \mathcal{M}[u_z^c(r) \cdot \overline{u_z^n(r)}] + \mathcal{M}[\overline{u_z^c(r)} \cdot u_z^n(r)] \right\} \cos \vartheta \\ &\quad + \left\{ \mathcal{M}[u_z^s(r) \cdot \overline{u_z^n(r)}] + \mathcal{M}[\overline{u_z^s(r)} \cdot u_z^n(r)] \right\} \sin \vartheta. \end{aligned} \quad (33)$$

These allow us to express some linear relationships between the variances of the ground motion component at the origin and the source components

$$\mathcal{V}_r(r, \vartheta) = (\mathcal{V}[\Psi_x] \cos^2 \vartheta + \mathcal{V}[\Psi_y] \sin^2 \vartheta) |\tilde{u}_r(r)|^2 + \mathcal{V}[\Psi_z] |u_r^*(r)|^2, \quad (34)$$

$$\mathcal{V}_\vartheta(r, \vartheta) = (\mathcal{V}[\Psi_y] \cos^2 \vartheta + \mathcal{V}[\Psi_x] \sin^2 \vartheta) |\tilde{u}_\vartheta(r)|^2, \quad (35)$$

$$\mathcal{V}_z(r, \vartheta) = (\mathcal{V}[\Psi_x] \cos^2 \vartheta + \mathcal{V}[\Psi_y] \sin^2 \vartheta) |\tilde{u}_z(r)|^2 + \mathcal{V}[\Psi_y] |u_z^*(r)|^2, \quad (36)$$

and some other relationships for covariances

$$\begin{aligned} \mathcal{K}_r(r, \vartheta) &= 2 |\tilde{u}_r(r)|^2 \cdot \mathcal{K}(\Psi_x, \Psi_y) \cos \vartheta \sin \vartheta \\ &\quad + 2 \Re \{ \tilde{u}_r(r) \cdot \overline{u_r^*(r)} \} \\ &\quad \cdot \{ \mathcal{K}(\Psi_x, \Psi_z) \cos \vartheta + \mathcal{K}(\Psi_y, \Psi_z) \sin \vartheta \}, \end{aligned} \quad (37)$$

$$\mathcal{K}_\vartheta(r, \vartheta) = -2 |\tilde{u}_\vartheta(r)|^2 \cdot \mathcal{K}(\Psi_x, \Psi_y) \cos \vartheta \sin \vartheta, \quad (38)$$

$$\begin{aligned} \mathcal{K}_z(r, \vartheta) &= 2 |\tilde{u}_z(r)|^2 \cdot \mathcal{K}(\Psi_x, \Psi_y) \cos \vartheta \sin \vartheta \\ &\quad - 2 \cdot \Re \{ \tilde{u}_z(r) \cdot \overline{u_z^*(r)} \} \\ &\quad \cdot \{ \mathcal{K}(\Psi_x, \Psi_z) \cos \vartheta + \mathcal{K}(\Psi_y, \Psi_z) \sin \vartheta \}. \end{aligned} \quad (39)$$

These results link the statistical properties of the source and those of the ground motion at the receiver.

## 2.2 The effect of distributed sources: ambient vibrations

In Arai & Tokimatsu (2004, 2005) and Lunedei & Albarello (2009), ambient vibrations are considered to be the effect of a multitude of independent and random point-like harmonic sources uniformly distributed on the Earth's surface. Maintaining this description, let us now consider a ring with radii  $r_1$  and  $r_2$  ( $r_2 > r_1 \geq 0$ )

$$\mathcal{C} \equiv \left\{ (x, y)^T \in \mathbb{R}^2 \mid r_1 \leq \sqrt{x^2 + y^2} \leq r_2 \right\}, \quad (40)$$

which is uniformly filled with independent, stochastic point-like harmonic sources and whose surface density is expressed by the function

$$\Phi e^{-i\omega t} = \begin{pmatrix} \Phi_x \\ \Phi_y \\ \Phi_z \end{pmatrix} e^{-i\omega t}. \quad (41)$$

Each Cartesian component of each source is characterized by vanishing average

$$\mathcal{M}[\Phi_x] = \mathcal{M}[\Phi_y] = \mathcal{M}[\Phi_z] = 0,$$

and by a surface variance and covariance densities

$$\mathcal{V}[\Phi_h] = \mathcal{M}[|\Phi_h|^2], \quad h = x, y, z,$$

$$\mathcal{K}(\Phi_h, \Phi_q) = \mathcal{M}[\Phi_h \cdot \overline{\Phi_q}], \quad h, q = x, y, z.$$

We also introduce the total surface variance density  $\sigma^2$  and those relative to the Cartesian normalized components  $\sigma_h^2$ , which are related via

$$\sigma \equiv \sqrt{\mathcal{V}[\Phi_x] + \mathcal{V}[\Phi_y] + \mathcal{V}[\Phi_z]},$$

$$\sigma_h \equiv \frac{\sqrt{\mathcal{V}[\Phi_h]}}{\sigma}, \quad h = x, y, z,$$

$$\sigma_x^2 + \sigma_y^2 + \sigma_z^2 = 1.$$

Since the sources are assumed to be independent, the total mean and variance of the displacements at the origin are simply given by the sum of those relative to each source (eqs 22–24, 26, 28 and 31). Thus, for each cylindrical component, the total mean is zero, while the total variance is the surface integral on  $\mathcal{C}$

$$\begin{aligned} \mathcal{V}_n^{\text{TOT}} &= \int_{\mathcal{C}} \mathcal{V}[u_n(r, \vartheta)] \, dx \, dy \\ &= \int_{r_1}^{r_2} \int_0^{2\pi} \mathcal{V}_n(r, \vartheta) r \, dr \, d\vartheta + \int_{r_1}^{r_2} \int_0^{2\pi} \mathcal{K}_n(r, \vartheta) r \, dr \, d\vartheta, \end{aligned} \quad (42)$$

for  $n = r, \vartheta, z$ . By using some known trigonometric integrals, one can see that all the angular integrals of the terms  $\mathcal{K}_n(r, \vartheta)$  vanish and thus

$$\begin{aligned} \mathcal{V}_r^{\text{TOT}}(\omega) &= \int_{r_1}^{r_2} \int_0^{2\pi} \mathcal{V}_r(r, \vartheta) r \, dr \, d\vartheta \\ &= \pi \sigma^2 \int_{r_1}^{r_2} \left\{ |\tilde{u}_r(r)|^2 (\sigma_x^2 + \sigma_y^2) + 2 |u_r^*(r)|^2 \sigma_z^2 \right\} r \, dr, \end{aligned} \quad (43)$$

$$\begin{aligned} \mathcal{V}_\vartheta^{\text{TOT}}(\omega) &= \int_{r_1}^{r_2} \int_0^{2\pi} \mathcal{V}_\vartheta(r, \vartheta) r \, dr \, d\vartheta \\ &= \pi \sigma^2 (\sigma_x^2 + \sigma_y^2) \int_{r_1}^{r_2} |\tilde{u}_\vartheta(r)|^2 r \, dr, \end{aligned} \quad (44)$$

$$\begin{aligned} \mathcal{V}_z^{\text{TOT}}(\omega) &= \int_{r_1}^{r_2} \int_0^{2\pi} \mathcal{V}_z(r, \vartheta) r \, dr \, d\vartheta \\ &= \pi \sigma^2 \int_{r_1}^{r_2} \left\{ |\tilde{u}_z(r)|^2 (\sigma_x^2 + \sigma_y^2) + 2 |u_z^*(r)|^2 \sigma_z^2 \right\} r \, dr. \end{aligned} \quad (45)$$

Note that the quantities  $\mathcal{V}_n^{\text{TOT}}(n = r, \vartheta, z)$  depend on  $\omega$  via the factors  $\tilde{u}_n(n = r, \vartheta, z)$  and  $u_n^*(n = r, z)$ , whose dependence is implicit in the functions  $L_H, R_{j,H}, R_{j,V}$  ( $j = 1, 2$ ) (remember eqs 17–21).

Obviously, one can change the physical space frame to compute the Cartesian components of the displacement (Appendix B), obtaining

$$\begin{aligned} \mathcal{V}_x^{\text{TOT}}(\omega) &= \sigma^2 \pi \int_{r_1}^{r_2} \left\{ \sigma_x^2 \left[ \frac{3}{4} (|\tilde{u}_r(r)|^2 + |\tilde{u}_\vartheta(r)|^2) \right. \right. \\ &\quad \left. \left. - \frac{1}{2} (\Re [\tilde{u}_r(r)] \Re [\tilde{u}_\vartheta(r)] + \Im [\tilde{u}_r(r)] \Im [\tilde{u}_\vartheta(r)]) \right] \right. \\ &\quad \left. + \frac{1}{4} \sigma_y^2 |\tilde{u}_r(r) + \tilde{u}_\vartheta(r)|^2 + \sigma_z^2 |u_r^*(r)|^2 \right\} r \, dr, \end{aligned} \quad (46)$$

$$\begin{aligned} \mathcal{V}_y^{\text{TOT}}(\omega) &= \sigma^2 \pi \int_{r_1}^{r_2} \left\{ \sigma_y^2 \left[ \frac{3}{4} (|\tilde{u}_r(r)|^2 + |\tilde{u}_\vartheta(r)|^2) \right. \right. \\ &\quad \left. \left. - \frac{1}{2} (\Re [\tilde{u}_r(r)] \Re [\tilde{u}_\vartheta(r)] + \Im [\tilde{u}_r(r)] \Im [\tilde{u}_\vartheta(r)]) \right] \right. \\ &\quad \left. + \frac{1}{4} \sigma_x^2 |\tilde{u}_r(r) + \tilde{u}_\vartheta(r)|^2 + \sigma_z^2 |u_r^*(r)|^2 \right\} r \, dr. \end{aligned} \quad (47)$$

Finally, we also note that, unlike the cylindrical case, the Cartesian variance components prove to be equal on both the horizontal directions [i.e.  $\mathcal{V}_x^{\text{TOT}}(\omega) = \mathcal{V}_y^{\text{TOT}}(\omega) \equiv \mathcal{V}_H^{\text{TOT}}(\omega)$ ] whenever the horizontal variance components are equal ( $\sigma_x = \sigma_y$ ).

These variances find a natural interpretation as the average power components of the signal at the receiver. *Ergo*, in the hypothesis  $\sigma_x = \sigma_y$ , the expected average spectral ratios HVSR can be computed in the form

$$HVSR(\omega) \equiv \sqrt{\frac{\mathcal{V}_H^{\text{TOT}}(\omega)}{\mathcal{V}_z^{\text{TOT}}(\omega)}}. \quad (48)$$

### 2.3 On the source features

As long as  $\Phi_h(h = x, y, z)$  are frequency independent, they can be interpreted as the Fourier component of a time delta function, that is, of an impulse at  $t = 0$ . Nevertheless, all previous formulae also hold if these components depend on the frequency, provided that their average value remains zero. In this case, the source power components become dependent on the frequency,  $\sigma(\omega)$  and  $\sigma_h(\omega)$ , and, whenever  $\sigma_x(\omega) \neq \sigma_y(\omega)$ , a suitable composition of  $\mathcal{V}_x^{\text{TOT}}$  and  $\mathcal{V}_y^{\text{TOT}}$  has to be chosen to obtain the horizontal power. In any case, our formulation is valid for any arbitrary time-dependent source.

Moreover, our formulae show that the HVSR does not depend on the total source power  $\sigma^2$  (which is reduced in eq. 48), but only on the power partition among the three space directions. This implies that the theoretical form of HVSR does not depend on the source–time function but on whether or not this results in a frequency-dependent power partition.

## 3 COMPUTATIONAL ASPECTS

Functions  $L_H$ ,  $R_{j,H}$  and  $R_{j,V}$  ( $j = 1, 2$ ) result from a sequence of products of layer matrices and their inverse ones, so they are computable in principle, but this computation is too troublesome in analytical form. Moreover, the integrations in  $k$  and  $r$  variables cannot be carried out in an analytical way. Thus, a numerical tool is necessary to execute computations in specialized cases.

*In primis*, given a fixed radius  $r$ , one deals with the computation of integrals (17)–(21), where the functions  $L_H$ ,  $R_{j,H}$  and  $R_{j,V}$  ( $j = 1, 2$ ) are known numerically only. By hypothesis, source and receiver points are at the same depth (at the Earth's surface), and this makes the  $k$  integrals very slow to converge. Hisada (1994, 1995) has provided an optimized numerical code to carry out the  $k$  integrations in eqs (6)–(13) for one source and a finite number of receivers. By setting a single source–receiver couple, we can use it to compute the integrals in question. In fact, calling the output of Hisada's code  $U_n$  ( $n = r, \vartheta, z$ ), we consider two fictitious source–receiver configurations (a horizontal and a vertical force)

- (1)  $\Psi_x = \Psi_y = 1$ ,  $\Psi_z = 0$ ,  $\vartheta = 0$ ; then  $\cos \vartheta = 1$ ,  $\sin \vartheta = 0$  and

$$\begin{cases} U_{rH}(r, 0, 0; 0) = \tilde{u}_r(r) \cdot \Psi_x = \tilde{u}_r(r) \\ U_{\vartheta H}(r, 0, 0; 0) = -\tilde{u}_\vartheta(r) \cdot \Psi_y = -\tilde{u}_\vartheta(r) \\ U_{zH}(r, 0, 0; 0) = \tilde{u}_z(r) \cdot \Psi_x = \tilde{u}_z(r) \end{cases} \quad (49)$$

- (2)  $\Psi_x = \Psi_y = 0$ ,  $\Psi_z = 1$ ,  $\vartheta = 0$ ; so

$$\begin{cases} U_{rV}(r, 0, 0; 0) = u_r^*(r) \cdot \Psi_z = u_r^*(r) \\ U_{\vartheta V}(r, 0, 0; 0) = 0 \\ U_{zV}(r, 0, 0; 0) = u_z^*(r) \cdot \Psi_z = u_z^*(r) \end{cases} \quad (50)$$

By inverting these relationships, the requested quantities are obtained

$$\begin{cases} |\tilde{u}_r(r)|^2 = |U_{rH}(r, 0, 0; 0)|^2 \\ |u_r^*(r)|^2 = |U_{rV}(r, 0, 0; 0)|^2 \end{cases} \quad (51)$$

$$|\tilde{u}_\vartheta(r)|^2 = |U_{\vartheta H}(r, 0, 0; 0)|^2 \quad (52)$$

$$\begin{cases} |\tilde{u}_z(r)|^2 = |U_{zH}(r, 0, 0; 0)|^2 \\ |u_z^*(r)|^2 = |U_{zV}(r, 0, 0; 0)|^2 \end{cases} \quad (53)$$

We made a single change to Hisada's code by adding the dispersion relationship (A4), which was lacking.

What remains to be done is the computation of the integrals in  $r$ . Since our aim is describing the ambient vibration wavefield, we have to face the problem of the integration limits. Differently to Lunedei & Albarello (2009), in the present formalization no *a priori* physical approximation is requested (only as concerns the dynamic wave equations) and thus we can safely set  $r_1 = 0$ . This implies that the contribution of the near sources can be accounted for. On the other hand, although the description adopted here includes the effect of internal friction by means of the complex functions  $L_H$ ,  $R_{j,H}$  and  $R_{j,V}$  ( $j = 1, 2$ ), the convergence of the integrals in the limit  $r_2 \rightarrow +\infty$  is not analytically demonstrable in the general case. Thus, this convergence has to be assumed without any proof on the basis of physical considerations only. Consequently, suitable upper integration limits, that is, a value of  $r_2$  at which the integral is assumed to have reached the convergence, have to be assumed in advance and the effectiveness of this choice has to be checked case by case.

Once a suitable value for the upper limit  $r_2$  has been fixed, a set of  $M$  points is chosen within the interval  $[0, r_2]$ :  $\{r_i\}_{i=1, \dots, M}$ . Then Hisada's code can run with  $r = r_i$  for each  $i = 1, \dots, M$  to evaluate the integrand functions at these radii. Finally, the integrals (43)–(47) can be computed with the simple trapezium rule.

Although this is a straightforward procedure, it requires a number of non-trivial choices. In fact, as formerly pointed out by Hisada (1994, 1995) and, for example, Herrmann (1979), the  $k$  integrands present some spikes for low  $k$  values, corresponding to Love and Rayleigh poles. As  $k$  increases, the same integrands present oscillating behaviours, which are dominated by the Bessel functions. Since the argument of Bessel functions is  $kr$ , these oscillations increase in frequency as  $r$  increases. This means that an increasing number of points in the  $k$  range is necessary to warrant an accurate estimate of the target function: for  $r$  values of the order of some kilometres, such an increase becomes so large that any possibility of effective computation is prevented. Actually, for a fixed density of  $k$  values, hard numerical instabilities appear for increasing values of  $r$  as an effect of the insufficient sampling in  $k$ . To prevent such a computational 'divergence', some reasonable limitation has to be imposed on the range of  $r$  values. In general, physical considerations suggest that the contribution of sources at the furthest distances should become negligible beyond any realistic distance (varying as a function of the frequency of interest and subsoil structure). This behaviour is actually observed in preliminary computations when the integrals begin to converge for  $r$  values that in most cases are of the order of some hundreds of metres from the receiver—well before the distance where numerical instabilities begin to appear. To exploit this feature, the sampling rate in  $k$  is fixed in advance, and computations in  $r$  are stopped when the contributions to the integral become negligible (i.e. below a fixed threshold value) as  $r$  increases. This, of course, implies a new 'tuning' parameter (the above-mentioned threshold value), whose effect on final computations should be evaluated case by case. In the following, the tuning parameter  $\tau$  has been set in the form

$$\frac{\int_r^{r+\Delta r} \mathcal{I}(\xi) d\xi}{\int_{r_1}^r \mathcal{I}(\xi) d\xi} < \tau \Delta r, \quad (54)$$

where  $\mathcal{I}(r)$  are the integrands in eqs (43)–(47). The integration is stopped when the above condition is satisfied by all integrals. The stopping values  $r_{\max}(\omega)$  can be considered an indicator of the area where the sources actually responsible for the ambient vibrations at the receiver are located.

Good results (in terms of smooth and stable HVSR curves) have been obtained by posing  $\Delta r = 100$  m and by assuming values for  $\tau$  in the range  $[10^{-5}, 10^{-4}]$  m<sup>-1</sup>.

In general, the evaluation of integrals (43)–(47) is computationally troublesome: typically, to obtain a good HVSR curve, several hours of CPU time are required on a standard desktop PC.

#### 4 APPLICATION EXAMPLES

In order to evaluate and exploit the performance of the above formulation, it was applied to three subsoil configurations.

The first, called ‘Profile M’ and shown in Table 1, was used by Bonnefoy-Claudet *et al.* (2006b) to evaluate expected HVSR shapes at a number of receivers in the frame of a purely numerical simulation of the ambient vibration wavefield. The profile is very simple, with one sharp impedance contrast in the  $V_S$  profile at a depth of 25 m; the expected resonance frequency is 2 Hz. In principle, the characteristics of this profile allow us to illustrate the properties of a high impedance contrast (about 6.5) between the sedimentary layer and the bedrock, for which it is known (e.g. Konno & Ohmachi 1998) that the ellipticity of the fundamental mode of Rayleigh waves is very close to the  $S$ -wave resonance frequency of the site.

The two other profiles, called ‘Profile A’ and ‘Profile B’ and shown in Tables 2 and 3, respectively, have been considered by Arai & Tokimatsu (2004) and Lunedei & Albarello (2009). As regards  $V_P$  and  $V_S$  values up to the depth of one hundred metres, the values in the tables were deduced from experimental data. Velocity values relative to deeper strata were deduced from crustal models (see Arai & Tokimatsu 2004 for details). Realistic values of the seismic quality factor and density were added by Lunedei & Albarello (2009).

**Table 1.** Seismic Profile M (Bonnefoy-Claudet *et al.* 2006b).

$H$ (m)	$V_P$ (m s <sup>-1</sup> )	$V_S$ (m s <sup>-1</sup> )	$\rho$ (kg m <sup>-3</sup> )	$Q_P$	$Q_S$
25	1350	200	1900	50	25
$\infty$	2000	1000	2500	100	50

**Table 2.** Seismic Profile A (Arai & Tokimatsu 2004; Lunedei & Albarello 2009).

$H$ (m)	$V_P$ (m s <sup>-1</sup> )	$V_S$ (m s <sup>-1</sup> )	$\rho$ (kg m <sup>-3</sup> )	$Q_P$	$Q_S$
5.5	1333	240	1900	20	10
3.6	1333	133	1900	22	11
4.6	1333	175	1900	24	12
6.3	1333	222	1900	26	13
20.0	1333	155	1900	28	14
4.6	1333	175	1900	30	15
6.4	1333	250	1900	32	16
9.0	1595	570	1900	34	17
23.6	1595	333	1900	36	18
16.4	1595	575	1900	38	19
1400.0	1800	700	1900	52	26
800.0	2800	1500	2200	60	30
$\infty$	5600	3000	2500	100	50

**Table 3.** Seismic Profile B (Arai & Tokimatsu 2004; Lunedei & Albarello 2009).

$H$ (m)	$V_P$ (m s <sup>-1</sup> )	$V_S$ (m s <sup>-1</sup> )	$\rho$ (kg m <sup>-3</sup> )	$Q_P$	$Q_S$
2.3	330	170	1900	20	10
4.8	740	165	1900	26	13
2.3	1015	355	1900	28	14
2.5	1015	330	1900	30	15
5.0	1800	460	1900	32	16
83.1	1800	625	1900	40	20
1400.0	1800	700	1900	62	31
800.0	2800	1500	2200	70	35
$\infty$	5600	3000	2500	100	50

Profile A presents a number of velocity inversions. In principle, in this profile, the upper propagation modes of surface waves are expected to play a major role. Four major impedance contrasts exist in the  $V_S$  profile at depths of 51, 84, 100 and 1500 m. The first is due to a relatively thin high-velocity layer (9 m), while the second is probably more important since it corresponds to a well-defined transition between an upper low-velocity zone (average  $V_S = 225$  m s<sup>-1</sup>) and deeper high-velocity strata.

Profile B is normally dispersive, that is, it presents an almost monotonic increase of  $V_S$  values with depth. A minor impedance contrast relative to  $V_S$  exists at the depth of 17 m, while the most important contrast is very deep (1500 m).

In all of the computations described in the following, the source characteristics have been assumed in the form

$$\sigma_x = \sigma_y = \frac{1}{2}, \quad \sigma_z = \frac{1}{\sqrt{2}}, \quad (55)$$

that is, the same used in Lunedei & Albarello (2009); in this case, as noted above,  $\mathcal{V}_H^{\text{TOT}}(\omega) = \mathcal{V}_x^{\text{TOT}}(\omega) = \mathcal{V}_y^{\text{TOT}}(\omega)$  holds and definition (48) is well given. This configuration assumes that horizontal and vertical source-density power are equal on average.

In the computation described in the following two subsections, the minimum integration radius  $r_1$  has been fixed at 0, that is, it is assumed that sources fill all the surface around the receiver. This choice, which in most cases can be considered unrealistic, was made in order to evaluate the possible role of near-source phases that have been completely disregarded in previous analyses. The resulting patterns will be considered as a benchmark for other models that will be presented later and where more realistic choices for the  $r_1$  will be considered.

The above model was applied to the three subsoil configurations in order to explore some aspects of the HVSR interpretation that are important for practical applications.

##### 4.1 HVSR versus $S$ -wave transfer function

In order to evaluate the possible role of HVSR in the practice of seismic zoning, the reliability of the relationship existing between HVSR and  $S$ -wave transfer function has to be assessed. In this regard, different positions exist especially with respect to the role of body waves in controlling frequency and amplitude of HVSR maxima (e.g. Bard 1999; Nakamura 2009). In particular, on the assumption that body waves play a major role, a strong analogy is expected between HVSR function and  $S$ -wave response function (e.g. Nakamura 2000, 2009; Herak 2008). To check this hypothesis, the expected  $S$ -wave transfer function was computed for the three subsoil profiles M, A and B (Fig. 1). As regards Profile M, the  $S$ -wave transfer function can be computed analytically (e.g. Kramer

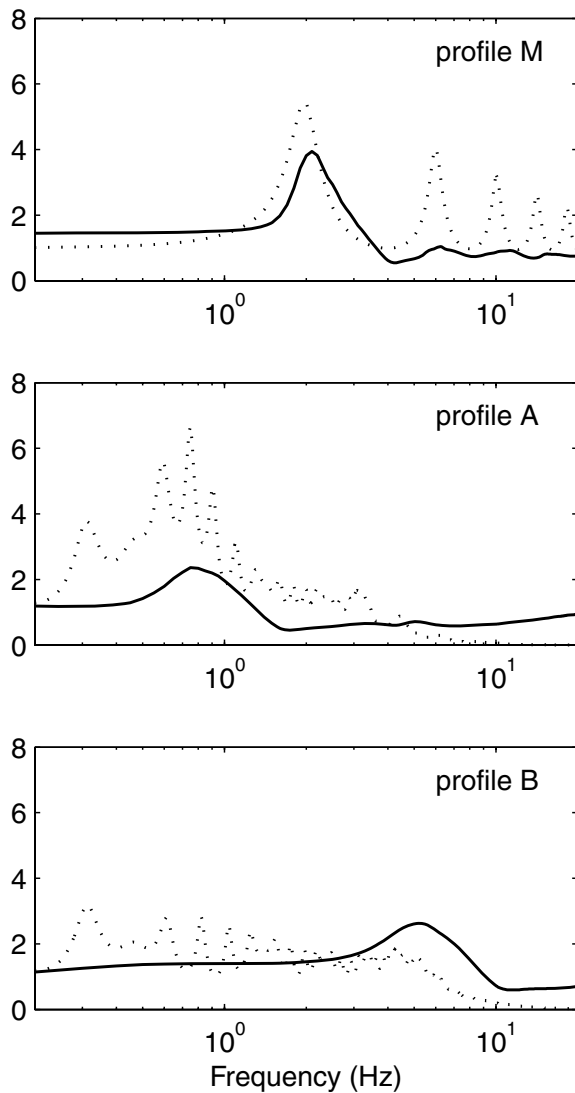


**Figure 1.** Response functions for  $V_S$  in the three profile in Tables 1–3 (dotted lines) compared with HVSR patterns relative to ambient vibration full wavefield ( $r_1 = 0$ ) (solid lines).

1996), while in the other cases, the numerical procedure provided by Tsai (1970) was used (see, e.g. Herak 2008). The resulting curves were compared with theoretical HVSR curves deduced for the three profiles by using the ambient vibration model based on full wavefield modelling.

As expected, the  $V_S$  response function relative to Profile M is relatively simple, with a large peak in correspondence with the fundamental resonance frequency (2 Hz) and several minor peaks relative to its higher-frequency multiplets. In this case, the expected HVSR mimics the  $S$ -wave response function with some important differences. The fundamental resonance frequency is well identified by the HVSR maximum. However, its amplitude is underestimated by about 30 per cent. A greater underestimate is obtained for secondary maxima of the transfer function, which are barely visible in the theoretical HVSR.

As regards Profile A (Table 2), response function appears less regular than in the previous case as the effect of a more complex  $V_S$  profile. A number of peaks below 1 Hz can be identified. In particular, three clear peaks are visible at 0.6, 0.75 and 0.9 Hz: the first and the last are probably representative of impedance contrasts

at 100 and 51 m depth, respectively. The 0.75 Hz peak might be associated with the velocity inversion at a depth of about 84 m, where a relatively sharp transition occurs between the shallow low-velocity zone and the deeper high-velocity layers. A further peak exists at around 0.3 Hz, which is the effect of the deeper impedance contrast (1500 m). The theoretical HVSR curve shows only one significant peak at around 0.75 Hz in good correspondence with the absolute maximum of the  $S$ -wave response function. Beyond this good match, however, the HVSR shape and the response function appear uncorrelated. In particular, no trace is found in the computed HVSR of the lower-frequency peaks at 0.3 and 0.6 Hz. Furthermore, the amplitude of the  $S$ -wave response function at 0.75 Hz is substantially underestimated by the HVSR curve.

Due to the lack of significant impedance contrasts, the response function relative to Profile B (Table 3) does not show large peaks. In this case, the HVSR curve shows a relatively small maximum at around 5 Hz, with an amplitude which is larger than the corresponding  $S$ -wave response function at the same frequency. HVSR does not show any signature of the other low-frequency maxima.

The above results confirm the idea that HVSR deduced from ambient vibrations does not represent the  $S$ -wave transfer function but reflects the position of the resonance frequency which is correctly detected when it corresponds to a significant seismic impedance contrast (see e.g. Haghshenas *et al.* 2008). In general, HVSR provides both overestimates and underestimates of the seismic response at the resonance frequency, depending on the specific subsoil configuration. This result is compatible with available empirical evidence (Haghshenas *et al.* 2008).

#### 4.2 The reliability of the surface wave approximation

To evaluate the feasibility of surface wave approximation for the computation of theoretical HVSR for ambient vibrations, theoretical HVSR curves deduced in the frame of the generalized surface wave approximation (Lunedei & Albarello 2009) were considered. In this model, too, ambient vibrations are assumed to be the effect of independent and random point sources located at the surface of the Earth. However, unlike the case of the full wavefield model (Section 2), only plane surface waves propagating with multimodal velocities are considered. On this basis, relatively fast computations are required to estimate expected ground-motion components as a function of the local  $V_S$ ,  $V_P$ , density and damping profiles. In particular, it is possible to compute the average power of vertical ( $P_z$ ), radial and transversal ( $P_r$  and  $P_\theta$ ) ground-motion components that can be interpreted as the Rayleigh (vertical and horizontal) and Love average contributions, respectively. In this approximation, the following relationships (Lunedei & Albarello 2009) were used to compute the expected HVSR curve

$$HVSR(\omega) \equiv \sqrt{\frac{P_H(\omega)}{P_z(\omega)}}, \quad (56)$$

where

$$P_H(\omega) \equiv \sqrt{P_r(\omega) \cdot P_\theta(\omega)}. \quad (57)$$

In this way, theoretical HVSR curves were computed for the three subsoil profiles, which were then compared with those obtained from the full wavefield model (Figs 2–4). In these computations, we considered all modes up to the fifteenth mode.

As regards Profile M (Fig. 2a), a very high HVSR peak is obtained from the surface wave approximation at the resonance frequency



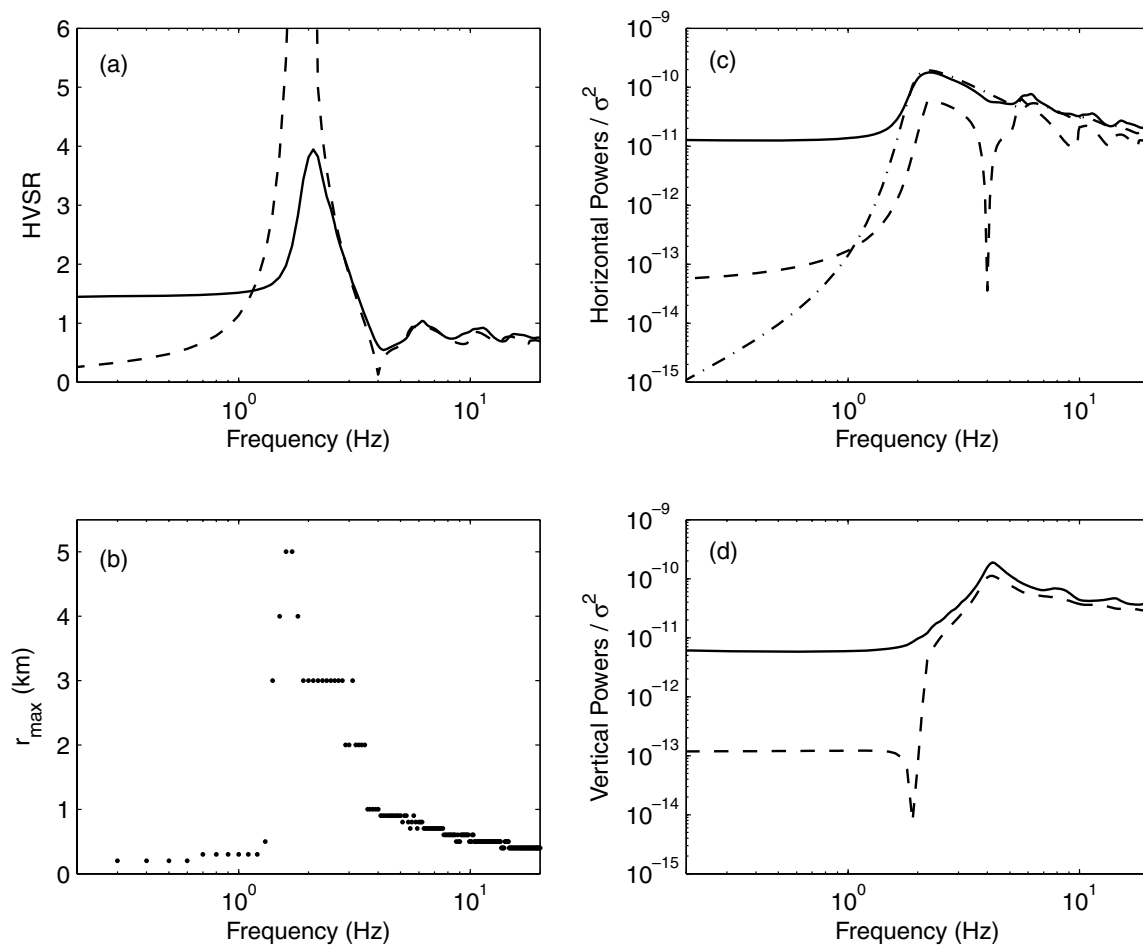


**Figure 2.** Comparison of theoretical curves relative to HVSr, power density and maximum source–receiver distance computed in the case of Profile M (Table 1) using the full wavefield model (Section 2) and those obtained for the same profile in the surface wave approximation (Lunedei & Albarello 2009). The full wavefield model was applied in accordance with the hypothesis that sources exist all around the receiver ( $r_1 = 0$ ). (a) HVSr pattern deduced from the full wavefield solution (solid line) compared with that relative to the surface wave approximation (dashed line); (b) maximum source–receiver distances ( $r_{\max}$ ); (c) average power densities of horizontal components of ambient vibrations deduced from the full wavefield solution (solid line) compared with the Love (dash–dotted line) and Rayleigh (dashed line) components; (d) average power densities of vertical components of ambient vibrations deduced from the full wavefield solution (solid line) compared with the Rayleigh wave component (dashed line).

(2 Hz). This is the effect of the sharp reduction of the power density relative to the vertical component of ambient vibration (Fig. 2d). The HVSr computed from the full wavefield model also shows a significant peak in correspondence with the resonance frequency, but its amplitude is much smaller than that provided by the surface wave approximation. In general, the two HVSr curves show good agreement in the range of frequencies above the resonance frequency, while a complete mismatch exists at and below this frequency. The examination of the corresponding power-density functions (Figs 2c and d) shows that the sharp maximum and the higher-frequency minimum in the HVSr deduced in the surface wave approximation are associated with deep minima linked to the ellipticity of Rayleigh waves (e.g. Fäh *et al.* 2001). These last minima prove to be ‘filled in’ by other seismic phases when the full wavefield model is considered. These phases appear to also play a major role in the low-frequency range ( $<2$  Hz), where the surface wave contribution becomes almost non-existent.

In the case of Profile A (Fig. 3a), the HVSr curve computed both by using the full wavefield solution and the surface wave approximation presents a clear maximum: however, these maxima are located at different frequencies (0.6 and 0.75 Hz, respectively). A rather

good degree of agreement exists above the resonance frequency, with an important discrepancy around 1.8 Hz where a relative maximum in one case corresponds to a relative minimum in the other. In this case, too, a complete disagreement exists for HVSr amplitudes at and below the resonance frequency. As regards the power-density functions (Figs 3c and d), an overall agreement exists between the patterns obtained in the surface wave approximation and in the full wavefield model. However, the respective amplitudes differ by about one order of magnitude.

Almost the same observations hold in the case of Profile B (Fig. 4a) with a more evident mismatch between the frequency of HVSr maxima (4 Hz versus 5 Hz). In this case also, a secondary HVSr maximum is deduced from surface wave approximation that corresponds to a minimum in the HVSr curve resulting from the full wavefield model. In the same way, the shape of power density functions determined by considering surface wave approximation and the full wavefield (Figs 4c and d) agree as concerns the overall shape but differ of about one order of magnitude.

Both in the cases of Profiles A and B, amplitudes of HVSr maxima deduced in the surface wave approximation tend to overestimate the values deduced from the full wavefield solution.

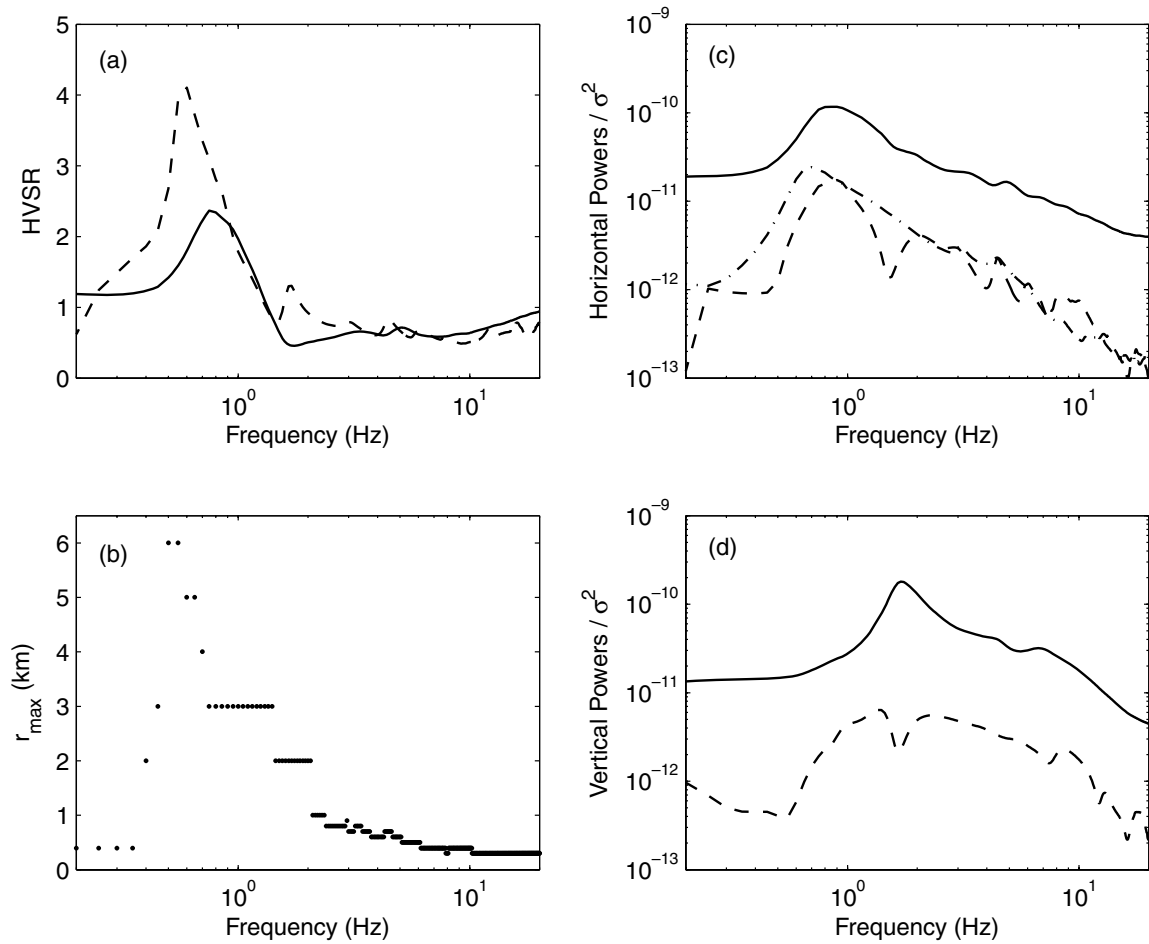


**Figure 3.** Comparison of theoretical curves relative to HVSR, power density and maximum source–receiver distance computed in the case of Profile A (Table 2) using the full wavefield model (Section 2) and those obtained for the same profile in the surface wave approximation (Lunedei & Albarello 2009). The full wavefield model was applied in accordance with the hypothesis that sources exist all around the receiver ( $r_1 = 0$ ). See caption of Fig. 2.

#### 4.3 The role of the source-free area

In general, the mismatch between results provided by the surface wave approximation and the full wavefield model can be attributed to two different factors that are strictly interconnected. The first is that, by definition, surface wave approximation disregards the role of other seismic phases (non-planar surface waves, body waves, etc.). The second concerns the distribution of sources around the receiver. In fact, in the full wavefield solution, a uniform distribution of random sources is assumed to fill all the space around the receiver.

In the case of the surface wave approximation, given that only plane surface waves are considered, near-source contributions must be discarded to warrant a coherent application of the formalism (Tokimatsu 1997). This implies that an area has to be chosen that is source free, that is, where no source of ambient vibrations is active. The dimensions of this area can be fixed in different ways (e.g. Arai & Tokimatsu 2004; Bonnefoy-Claudet *et al.* 2006b; Lunedei & Albarello 2009), each being reasonable but essentially arbitrary. In the following, and in accordance with our previous work (Lunedei & Albarello 2009), the radius of such a source-free area is the characteristic average wavelength

$$\lambda_{\text{ave}}(\omega) = \frac{2\pi}{\omega} \langle V_S \rangle = \frac{2\pi}{\omega} \frac{\sum_{l=1}^{Z-1} H(l)}{\sum_{l=1}^{Z-1} H(l)/V_S(l)}, \quad (58)$$

where summation is carried out on the number of strata  $Z$ , each one characterized by a thickness  $H$  and a surface wave velocity  $V_S$ . This choice implies that  $\lambda_{\text{ave}}$  inversely depends on the frequency. As an example, in the cases of the three profiles M, A and B, this value relative to the frequency of 1 Hz corresponds to 100, 400 and 70 m, respectively.

It is reasonable to expect that near sources excluded in the approximate computations supply an important energy contribution and particular seismic phases to the wavefield that are discarded in the surface wave approximation. One effect of these latter phases is the larger power densities provided by the full wavefield model and the ‘filling up’ of Rayleigh wave minima.

The above considerations suggest that near sources play a major role in the shape of expected HVSR curves. In order to better evaluate this aspect, the full wavefield solution was computed by considering a source-free area around the receiver. Specifically, it was computed by assuming values of  $r_1$  that change with frequency in accordance with eq. (58). The results of these computations are reported in the left-hand column of Fig. 5. A significant change is obtained in the shape of HVSR with respect to the case with  $r_1 = 0$ . Furthermore, one can see that the mismatch between the HVSR computed in the surface wave approximation and that deduced from the full wavefield model with a frequency-dependent source-free area significantly decreases for all three profiles. In particular, a better correspondence is found between amplitude and

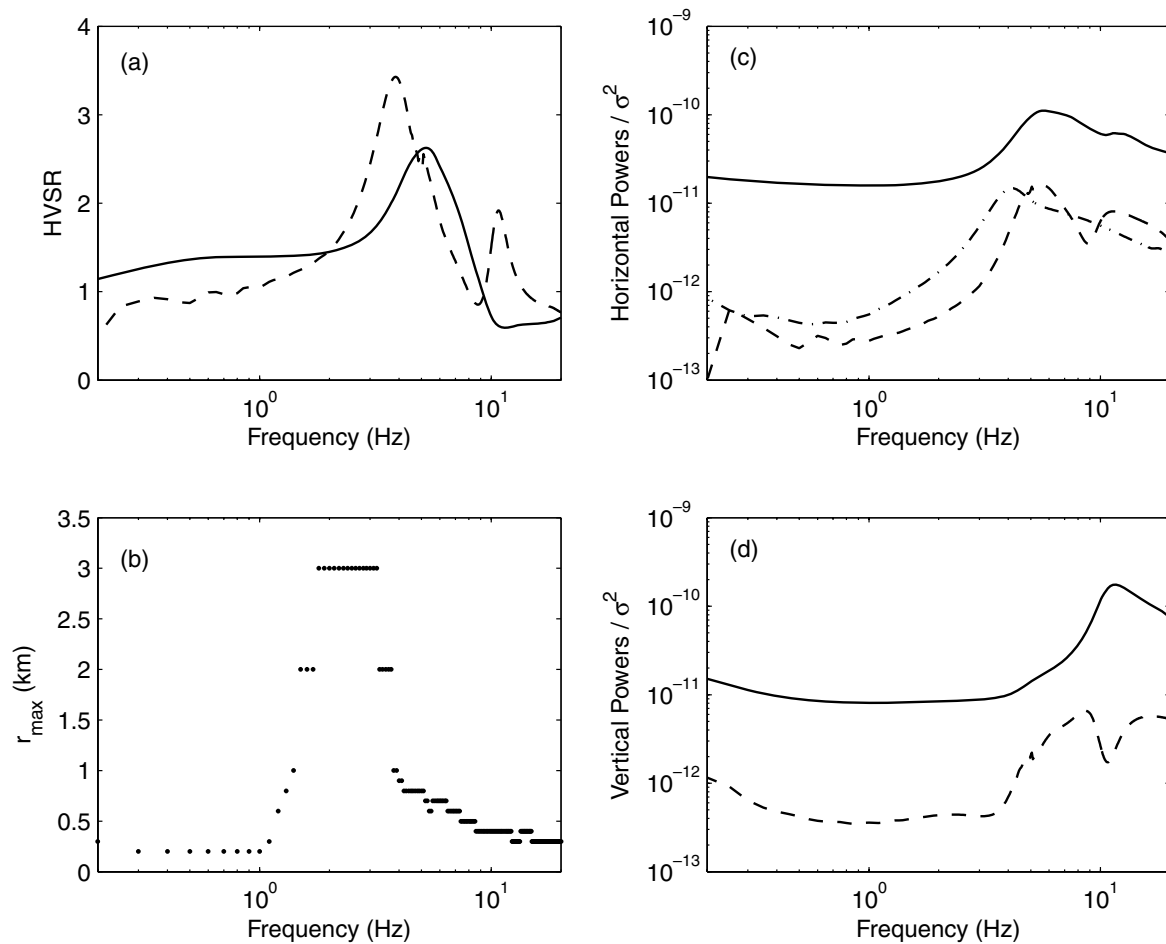


**Figure 4.** Comparison of theoretical curves relative to HVSR, power density and maximum source–receiver distance computed in the case of Profile B (Table 3) using the full wavefield model (Section 2) and those obtained for the same profile in the surface wave approximation (Lunedei & Albarello 2009). The full wavefield model was applied in accordance with the hypothesis that sources exist all around the receiver ( $r_1 = 0$ ). See caption of Fig. 2.

position of HVSR maxima. These findings suggest that the distribution of sources just around the receiver can strongly affect the shape of the HVSR curve. The above results confirm that in the far-field approximation it is possible to reconstruct wavefields that are similar to those calculated with wavenumber integral approaches, provided that many higher modes are included in the normal mode computations. However, when sources get closer and closer, such reconstruction becomes increasingly weak.

This subject becomes very interesting when one considers the applications for inversion protocols. The full wavefield solution for the modelling of HVSR is numerically troublesome (several hours for each run on a standard PC) and this prevents its application in numerical inversion procedures used to infer the seismic layering of the subsoil from experimental HVSR curves (see, e.g. Scherbaum *et al.* 2003; Arai & Tokimatsu 2004; Parolai *et al.* 2005; Picozzi & Albarello 2007). Thus, the use of suitable numerical approximations is mandatory for the provision of feasible inversion protocols. To this end, an attempt was carried out to evaluate the feasibility of the surface wave approximation (in the form proposed by Lunedei & Albarello 2009). The results obtained indicate that such approximation provides fairly good results in the range of frequencies above the resonance frequency. The feasibility of this approximation can be improved if a source-free area (with a radius of a few tens of metres) exists around the receiver. To demonstrate this, full wavefield solutions for the three profiles were computed by con-

sidering different source-free areas around the receiver. The choice of a frequency-independent source-free area aims at simulating a realistic experimental situation where possible sources can actually be eliminated around the receiver (e.g. by choosing a site relatively far from roads or other noise sources). Three different radii of the source-free area were considered: 10 m, 50 and 100 m. The results obtained for the three subsoil profiles are shown in the right-hand panels of Fig. 5. One can see that the feasibility of the surface wave approximation rapidly improves when a source-free area of a few tens of metres is considered: in fact, the HVSR curves from the full wavefield model rapidly converge with those from the surface wave approximation. These findings suggest that if a source-free area exists around the receiver, inversion procedures based on the surface wave approximation for the direct modelling of empirical HVSR curves can be used to constrain the body wave (mainly *S*) velocity and damping profile in the subsoil. In the other cases, due to its sensitivity to near sources, caution is required in the interpretation of HVSR at and below the resonance frequency in terms of subsoil mechanical configuration alone.

#### 4.4 A ‘skin’ effect for random vibrations

The plots of  $r_{\max}$  values relative to the different frequencies for the three subsoil configurations (Figs 2b, 3b and 4b) indicate that

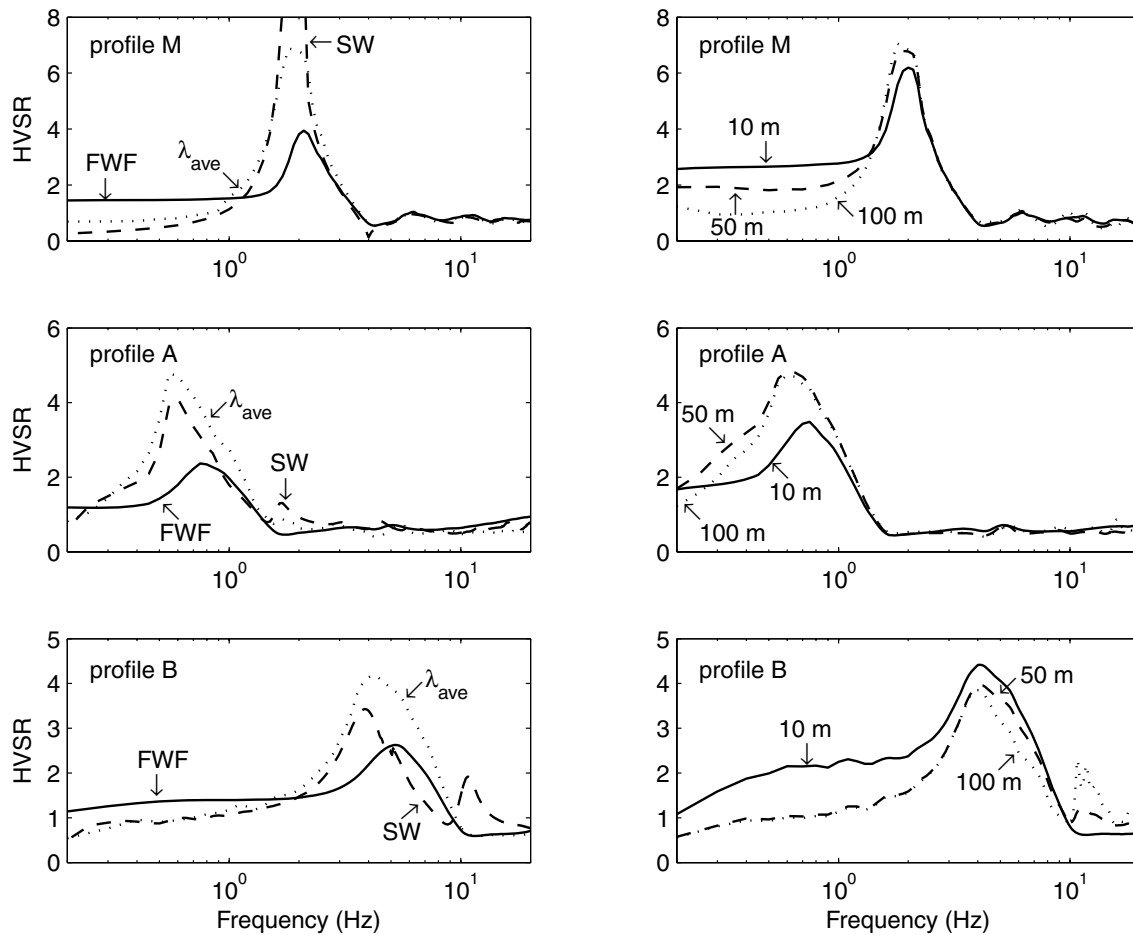


**Figure 5.** Comparison of theoretical HVSR curves relative to the three profiles in Tables 1–3 computed by following the full wavefield model (Section 2) by assuming different radii  $r_1$  of a circular, source free-area around the receiver. Theoretical HVSR curves computed in the surface wave approximation (Lunedei & Albarello 2009) are also reported for comparison. On the left-hand side, the comparison is shown between the theoretical HVSR deduced in the surface wave approximation ('SW'), using the full wavefield model with  $r_1 = 0$  ('FWF'), and the same model with  $r_1 = \lambda_{ave}(\omega)$  in eq. (58) ( $\lambda_{ave}$ ). On the right-hand side, theoretical HVSR curves computed using the full wavefield model with frequency-independent values of  $r_1$  (in the labels) are reported.

in the correspondence of the low- and high-frequency bands,  $r_{max}$  values sharply decrease to values of the order of a few hundreds of metres. This implies that local sources play a major role both as concerns the low- and the high-frequency bands. With respect to high frequencies, this pattern can be reasonably interpreted as the effect of material damping. By contrast, this interpretation fails for low frequencies (below the resonance frequency), because in this case, the role of very distant sources should turn out to be enhanced.

To explain this pattern, a sort of 'skin' effect can be hypothesized that concerns the spectral amplitudes of surface waves in layered media. A strong reduction of surface wave amplitude below the resonance frequency was highlighted by Scherbaum *et al.* (2003) and is confirmed by our computations (see the dramatically declining power spectral densities relative to the surface wave approximation in Figs 2–4). A possible interpretation of the observed effect is that the presence of a sharp variation in the  $V_s$  profile induces energy-trapping phenomena between the surface (where the noise originates) and the impedance contrast at depth, which result in high-pass filtering of the surface wavefield. In fact, since the penetration depth of surface waves depends on the frequency (Aki & Richards 1980), energy trapping in the shallowest part of the subsoil due to the presence of a sharp impedance contrast at the basis of soft sediments is expected to affect the surface wave spectrum by

transferring energy from low-frequency (more depth-penetrating) to high-frequency (less depth-penetrating) components. The frequency boundary between the enhanced and damped spectral components is expected to correspond to the resonance frequency of the soft sedimentary layer that identifies the range of frequency involved in the energy-trapping process. Instead, the amount of the energy transfer is a function of the sharpness of the impedance contrast at the bottom of the low-velocity layer. Both these statements are corroborated by the results shown in Figs 2–4.

To evaluate the role of this phenomenon, we must return to the results in Fig. 1, where we note that in the presence of multiple, significant impedance contrasts, the shallower one only seems to affect the corresponding HVSR curve. The examination of the power densities relative to the three profiles (subplots c and d in Figs 2–4) indicates that below the resonance frequency, the power density computed by considering the full wavefield associated with both the vertical and horizontal components undergoes a significant lowering (of about one order of magnitude or more) with respect to the relevant maximum value. This lowering becomes much more evident when only surface waves are considered. This implies that high-pass filtering mostly affects surface waves. An effect of this filtering is that only very near sources (which supply the most energetic contributions) are responsible for ambient vibrations in the

low-frequency band, at least as far as local random sources as concerned. A second result is that an intrinsic difficulty exists with using HVSR to obtain information about the deep  $V_S$  profile below the first strong impedance contrast.

## 5 CONCLUSIONS

A physical model for ambient vibrations in a weakly dissipative layered Earth was developed. This model can be considered an analytic generalization to a continuous distribution of random, independent sources of the numerical procedures previously applied by other authors (Bonnefoy-Claudet *et al.* 2006b) to the case of a finite number of localized sources.

The model is based on the full wavefield solution relative to harmonic point loads applied at the surface of the Earth. The choice of uncorrelated, surface point loads can be considered a reliable representation of anthropic sources (Bonnefoy-Claudet *et al.* 2006b) and thus, the above model is only representative of ambient vibrations in the range of engineering interest (approximately [0.5, 20] Hz), where local point sources mainly of anthropic origin dominate the tremor (Bonnefoy-Claudet *et al.* 2006a). In order to include the effect of large-scale noise sources responsible for low-frequency noise (e.g. oceanic storms, barometric variations, sea-wave interference), a quite different source model should be considered that, for example, takes into account long-range correlation between surface sources.

From this physical core, the average power of ambient vibrations was computed as the effect of a continuous, uniform distribution of random, independent sources all around the receiver. In this model, average powers relative to ground-motion components can be computed as a linear function of the average features of the point loads responsible for the wavefield. Based on the assumption that horizontal and vertical source components have the same average power, a number of features of the expected wavefield were obtained in terms of integrals that, in specialized cases, have to be solved numerically. In particular, the expected properties of HVSR were focused on due to their practical significance in seismic engineering.

The results obtained from the application of the model proposed here to a set of subsoil configurations are compatible with observations (e.g. Haghshenas *et al.* 2008) and results emerging from numerical simulations (Bonnefoy-Claudet *et al.* 2006b). For example, is the model confirmed the reliability of HVSR from ambient vibrations for detecting resonance phenomena induced by the presence of significant  $S$  wave impedance contrasts in the subsoil. Furthermore, HVSR maxima appear to correlate well with resonance frequency relative to the shallower, strong impedance contrast ( $>2$ ) in the subsoil. Due to the limited number of configurations considered here, these last results cannot be generalized, but they are in line with previous findings (e.g. Haghshenas *et al.* 2008). On the other hand, the presence of shallow, significant  $S$  wave impedance contrasts limits the penetration of vibrations generated at the surface by local incoherent random sources: this energy trapping in the shallower layers acts as high-pass filter for random vibrations by strongly reducing the power relative to frequencies below the resonance frequency. Of course, this conclusion cannot hold in the case of low-frequency ambient vibrations (microseisms) generated by different sources such as the remote storms analysed by Marzorati & Bindi (2006).

The frequency location of HVSR maxima is not necessarily linked to Rayleigh ellipticity since other seismic phases are probably present. On the other hand, resonant  $S$  and  $P$  body waves alone

are unable to explain HVSR amplitudes. In fact, no clear correspondence was found between HVSR amplitude values and  $S$  wave response function: in the three cases considered here, both overestimates and underestimates of the soil seismic response were revealed.

An important finding concerns the role of source distribution around the receiver. The relative importance of sources located at different distances from the receiver can be evaluated by considering stopping values ( $r_{\max}$ ) relative to the different frequencies for the three subsoil configurations (Figs 2b, 3b and 4b). These values can be considered as an estimate of the radius of the circular area around the receiver that includes the sources mostly responsible for ambient vibrations at each frequency. The values range from between a few kilometres (around the resonance frequency) down to a few hundreds of metres at low and high frequencies (i.e. below and above the resonance frequency). As regards the high-frequency range, the importance of near sources can be attributed to the effect of material damping. A 'skin' effect, responsible for low-frequency attenuation of surface waves, is responsible for the major importance of local sources in the low-frequency range.

These results indicate that, at least for the three profiles considered here, local sources, that is, those located in the range of a few hundreds of metres from the receiver, play a major role. As an example, the presence of sources all around the receiver results in HVSR pattern that are significantly different from those obtained when a source-free area exists. This implies that non-stationary fluctuations in the source distribution can be responsible for non-stationary HVSR curves.

Since the full wavefield solution is numerically too troublesome to be applied in numerical inversion procedures, the use of suitable numerical approximations is mandatory for providing feasible inversion protocols. We verified that the feasibility of this approximation can be improved if a source-free area (with a radius of a few tens of metres) exists around the receiver. These findings suggest that if a source-free area exists around the receiver, inversion procedures based on surface wave approximation for the direct modelling of empirical HVSR curves can be used to constrain the body wave (mainly  $S$ ) velocity and damping profile in the subsoil, at least as regards the high-frequency range ( $>0.5$  Hz), where ambient vibrations are dominated by local anthropic sources.

## ACKNOWLEDGMENTS

The authors thank Prof Marijan Herak, who kindly supplied the numerical code for the computation of  $S$  wave response function in a weakly dissipative layered Earth. The authors also thank the anonymous referees for their comments, which contributed to improving the work.

## REFERENCES

- Aki, K., 1957. Space and time spectra of stationary stochastic waves, with special reference to microtremors, *Bull. Earthq. Res. Inst.*, **XXXV**(part 3), 415–457.
- Aki, K. & Richards, P.G., 1980. *Quantitative Seismology - Theory and Methods*, Vol. I, ed. Freeman & C., San Francisco, USA.
- Arai, H. & Tokimatsu, K., 2004. S-wave velocity profiling by inversion of microtremor H/V spectrum, *Bull. seism. Soc. Am.*, **94**(1), 53–63.
- Arai, H. & Tokimatsu, K., 2005. S-wave velocity profiling by joint inversion of microtremor dispersion curve and horizontal-to-vertical (H/V) spectrum, *Bull. seism. Soc. Am.*, **95**(5), 1766–1778.

- Bard, P.-Y., 1999. Microtremor measurements: A tool for site effect estimation? *The Effects of Surface Geology on Seismic Motion*, pp. 1251–1279, eds Irikura, K., Kudo, K., Okada, H. & Sasatani T., Balkema, Rotterdam.
- Ben-Menahem, A. & Singh, S.J., 2000. *Seismic Waves and Sources*, Dover Publications Inc., New York, pp. 1102.
- Bonnefoy-Claudet, S., Cotton, F. & Bard, P.-Y., 2006a. The nature of noise wavefield and its applications for site effects studies: a literature review, *Earth Sci. Rev.*, **79**, 205–227.
- Bonnefoy-Claudet, S., Cornou, C., Bard, P.-Y., Cotton, F., Moczo, P., Kristek, J. & Fäh, D., 2006b. H/V ratios: a tool for site effects evaluation. Results from 1-D noise simulations, *Geophys. J. Int.*, **167**, 827–837.
- Bonnefoy-Claudet, S., Köhler, A., Cornou, C., Wathélet, M. & Bard P.-Y., 2008. Effects of love waves on microtremor H/V Ratio, *Bull. seism. Soc. Am.*, **98**(1), 288–300.
- D'Amico, V., Picozzi, M., Baliva, F. & Albarello, D., 2008. Ambient noise measurements for preliminary site-effects characterization in the urban area of Florence. *Bull. seism. Soc. Am.*, **98**(3), 1373–1388, doi:10.1785/0120070231.
- EVG1-CT-2000-00026 SESAME: Site Effects Assessment using Ambient Excitations [SESAME] European project, <http://sesame-fp5.obs.ujf-grenoble.fr/index.htm>, last accessed March 2008.
- Fäh, D., Kind, F. & Giardini, D., 2001. A theoretical investigation of average H/V ratios, *Geophys. J. Int.*, **145**, 535–549.
- Ferrari, G., Albarello, D. & Martinelli, G., 2000. Tromometric measurements as a tool for crustal deformation monitoring. *Seismol. Res. Lett.*, **71**(5), 562–569.
- Haghshenas, E., Bard, P.-Y. & Theodulis, N., 2008. Empirical evaluation of microtremor H/V spectral ratio, *Bull. Earthq. Eng.*, **6**, 75–108.
- Harkrider, D.G., 1964. Surface waves in multilayered elastic media, part 1, *Bull. seism. Soc. Am.*, **54**(2), 627–679.
- Herrmann, R.B., 1979. SH-wave generation by dislocation sources—a numerical study, *Bull. seism. Soc. Am.*, **69**(1), 1–15.
- Herak, M., 2008. ModelHVSR - a Matlab tool to model horizontal-to-vertical spectral ratio of ambient noise, *Comp. Geosci.*, **34**, 1514–1526.
- Hisada, Y., 1994. An efficient method for computing Green's functions for a layered half-space with sources and receivers at close depths. *Bull. seism. Soc. Am.*, **84**(5), 1456–1472.
- Hisada, Y., 1995. An efficient method for computing Green's functions for a layered half-space with sources and receivers at close depths (Part 2). *Bull. seism. Soc. Am.*, **85**(4), 1080–1093.
- Konno, K. & Ohmachi, T., 1998. Ground-motion characteristics estimated from spectral ratio between horizontal and vertical components of microtremor. *Bull. seism. Soc. Am.*, **88**(1), 228–241.
- Kramer, S.L., 1996. *Geotechnical Earthquake Engineering*, Prentice Hall, New Jersey, pp. 653.
- Lai, C.G. & Rix, G.J., 1998. *Simultaneous Inversion of Rayleigh Phase Velocity and Attenuation for Near-Surface Site Characterization*, Georgia Institute of Technology, USA.
- Lai, C.G. & Rix, G.J., 2002. Solution of the Rayleigh eigenproblem in viscoelastic media, *Bull. seism. Soc. Am.*, **92**(6), 2297–2309.
- Lachet, C. & Bard, P.-Y., 1994. Numerical and theoretical investigations on the possibilities and limitations of Nakamura's technique, *J. geophys. Earth*, **42**, 377–397.
- Lunedei, E. & Albarello, D., 2009. On the seismic noise wave field in a weakly dissipative layered Earth. *Geophys. J. Int.*, **177**, 1001–1014, doi:10.1111/j.1365-246X.2008.04062.x.
- Malishevsky, P.G. & Scherbaum, F., 2004. Love's formula and H/V-ratio (ellipticity) of Rayleigh waves. *Wave Motion*, **40**, 57–67.
- Marzorati, S. & Bindi, D., 2006. Ambient noise levels in Northern Italy. *Geochem. Geophys. Geosyst.*, **7**, Q09010, doi:10.1029/2006GC001256.
- Mucciarelli, M., Herak, M. & Cassidy, J., (eds), 2009. *Increasing Seismic Safety by Combining Engineering Technologies and Seismological Data* (NATO Science for Peace and Security Series C: Environmental), Springer, XVIII, pp. 382, ISBN: 978-1-4020-9194-0.
- Nakamura, Y., 1989. A method for dynamic characteristics estimation of subsurface using microtremor on the ground surface, *Quart. Rep. Railway Tech. Res. Inst.*, **30**(1), 25–33.
- Nakamura, Y., 2000. Clear identification of fundamental idea of Nakamura's technique and its applications, *Proceedings of the 12th World Conference on Earthquake Engineering*, Auckland, New Zealand, paper 2656.
- Nakamura, Y., 2009. Basic Structure of QTS (HVSR) and Examples of Applications. In *Increasing Seismic Safety by Combining Engineering Technologies and Seismological Data* (NATO Science for Peace and Security Series C: Environmental), eds Mucciarelli M. *et al.*, Springer, XVIII, 33–51.
- Okada, H., 2003. The microtremor survey method, *Gephys. Monogr. Series*, **12**, Society of Exploration Geophysicists, 135.
- Parolai, S., Picozzi, M., Richwalski, S.M. & Milkereit, C., 2005. Joint inversion of phase velocity dispersion and H/V ratio curves from seismic noise recordings using a genetic algorithm, considering higher modes, *Geophys. Res. Lett.*, **32**, doi:10.1029/2004GL021115.
- Picozzi, M. & Albarello, D., 2007. Combining Genetic and Linearized algorithms for a two-step joint inversion of Rayleigh wave dispersion and H/V spectral ratio curves, *Geophys. J. Int.*, **169**, 189–200.
- Scherbaum, F., Hinzen, K.-G. & Ohrnberger, M., 2003. Determination of shallow shear wave velocity profiles in the Cologne, Germany area using ambient vibrations, *Geophys. J. Int.*, **152**, 597–612.
- Tanimoto, T., 2008. Normal-mode solution for the seismic noise cross-correlation method. *Geophys. J. Int.*, **175**, 1169–1175.
- Tokimatsu, K., 1997. Geotechnical site characterization using surface waves, in *Proceedings of the 1st International Conference Earthquake Geotechnical Engineering*, eds Ishihara, K., pp. 1333–1368, A.A. Balkema, Brookfield, VT.
- Tsai, N.C., 1970. A note on the steady-state response of an elastic half-space. *Bull. seism. Soc. Am.*, **60**, 795–808.
- Wenzel, H. & Pichler, D., 2005. *Ambient Vibration Monitoring*, John Wiley & Sons Ltd, Chichester.

## APPENDIX A

Supposing that the force acting on the point  $(r, \vartheta, 0)^T$  is

$$\Psi_{\mathbf{q}} e^{-i\omega t}, \quad (\text{A1})$$

with a fixed  $\omega$  and with  $\mathbf{q}$  representing one of the principal directions  $\hat{\mathbf{x}}, \hat{\mathbf{y}}, \hat{\mathbf{z}}$  in such a way that one considers three forces along these directions

$$\begin{aligned} \Psi_{\hat{\mathbf{x}}} &\equiv (\Psi_{\hat{\mathbf{x}}}, 0, 0)^T \in \mathbb{C}^3 \\ \Psi_{\hat{\mathbf{y}}} &\equiv (0, \Psi_{\hat{\mathbf{y}}}, 0)^T \in \mathbb{C}^3 \\ \Psi_{\hat{\mathbf{z}}} &\equiv (0, 0, \Psi_{\hat{\mathbf{z}}})^T \in \mathbb{C}^3. \end{aligned} \quad (\text{A2})$$

In this hypothesis, it is possible to establish the dependence of the surface-motion amplitudes  $L_1, R_1, R_2$  on the force components  $\Psi_{\hat{\mathbf{x}}}, \Psi_{\hat{\mathbf{y}}}, \Psi_{\hat{\mathbf{z}}}$ .

In *primis*, one observes that this formulation takes into account the effects of the internal friction by using complex Lamé parameters, that is, complex body wave velocities. Following Lai & Rix (1998, 2002), on the assumption that material damping  $D_{\gamma}$  ( $D_{\gamma} = \frac{1}{2Q_{\gamma}}$ ,  $\gamma = P, S$  for  $P$  and  $S$  waves, respectively) is small ( $\leq 5$  per cent), the presence of anelastic attenuation can be simulated by assuming the Earth to be a layered viscoelastic body. In this case, the body wave velocities in the stratum  $j$  become complex and frequency dependent in the form

$$\begin{cases} \alpha^j(\omega) = V_P^j(\omega) \cdot [1 - i D_P^j] \in \mathbb{C} \\ \beta^j(\omega) = V_S^j(\omega) \cdot [1 - i D_S^j] \in \mathbb{C} \end{cases}, \quad (\text{A3})$$

for  $P$  and  $S$  waves, respectively, for all  $j = 1, \dots, N+1$ . The (real) quantities  $V_\gamma^j$  are given by the following dispersion relationships:

$$V_\gamma^j(\omega) = \frac{(V_\gamma^e)^j}{1 - \frac{2D_\gamma^j}{\pi} \log\left(\frac{\omega}{\omega_{\text{ref}}}\right)}, \quad (\text{A4})$$

where  $(V_\gamma^e)^j$  are the body wave velocities of the corresponding elastic media and  $\omega_{\text{ref}}/2\pi$  is the material reference frequency, usually equal to 1 Hz. Equation (A3) only holds at first-order approximation in  $D_\gamma^j$ .

In the following, we assume that  $\omega$  is fixed, so we drop this dependence.

### A1 SH waves

In each layer  $j$ , it is known (see, e.g. Aki & Richards 1980) that the SH amplitudes can be expressed by

$$\begin{pmatrix} L_1^j(z; k) \\ L_2^j(z; k) \end{pmatrix} = \mathbf{P}_L(z^N, z; k) \cdot \begin{pmatrix} 1 \\ -\mu^{N+1} \cdot v^{N+1} \end{pmatrix} \cdot C, \quad (\text{A5})$$

where  $\mathbf{P}_L(z_1, z_2; k)$  is the propagator matrix between the depths  $z_1$  and  $z_2$ ,  $C$  is a constant fixed by initial condition and

$$v^{N+1} \equiv \left[ k^2 - \left( \frac{\omega}{\beta^{N+1}} \right)^2 \right]^{\frac{1}{2}}.$$

By using Hisada's (1994) (A24, A25, A28), the surface load (A2) is represented by a stress discontinuity

$$L_2^1(0; k) \equiv L_0(k) = \begin{cases} l^*(k) \cdot \Psi_x, & \text{if } \mathbf{q} = \hat{\mathbf{x}} \\ l^*(k) \cdot \Psi_y, & \text{if } \mathbf{q} = \hat{\mathbf{y}} \end{cases},$$

with  $l^*(k) \equiv -\frac{k}{2\pi}$ . Then, if one calls

$$\mathbf{P}_L(z^N, 0; k) \equiv \begin{pmatrix} P_1 & P_2 \\ P_3 & P_4 \end{pmatrix},$$

we obtain

$$\begin{aligned} L_0(k) &= (0, 1) \cdot \mathbf{P}_L(z^N, 0; k) \cdot \begin{pmatrix} 1 \\ -\mu^{N+1} v^{N+1} \end{pmatrix} \cdot C \\ &= (0, 1) \cdot \begin{pmatrix} P_1 - \mu^{N+1} v^{N+1} \cdot P_2 \\ P_3 - \mu^{N+1} v^{N+1} \cdot P_4 \end{pmatrix} \cdot C \\ &= (P_3 - \mu^{N+1} \cdot v^{N+1} \cdot P_4) \cdot C = F_L(k) \cdot C, \end{aligned}$$

where  $F_L(k)$  is the Love secular function. It has been demonstrated (Aki & Richards 1980) that, for a layered half-space,  $F_L(k) = 0$  for a finite number of  $k$ s only: these solutions are the wavenumber of Love waves. Thus, with  $F_L(k) \neq 0$  for almost each  $k$ , then

$$C = \frac{L_0(k)}{F_L(k)} = \frac{l^*(k)}{F_L(k)} \Psi_h, \quad k - \text{a.e.},$$

for  $h = x, y$ , so (A5) one has

$$L_1^1(0; k) = \frac{P_1 - \mu^{N+1} v^{N+1} P_2}{F_L(k)} l^*(k) \Psi_h, \quad k - \text{a.e.},$$

for  $h = x, y$ . Thus, given

$$L_H(k) \equiv (P_1 - \mu^{N+1} v^{N+1} P_2) l^*(k),$$

one obtains that the displacement component is a linear function of the force

$$L_{1,x}(k) = L_H(k) \cdot \Psi_x, \quad k - \text{a.e.}$$

$$L_{1,y}(k) = L_H(k) \cdot \Psi_y, \quad k - \text{a.e.}$$

It is worth pointing out that the effect of the viscosity is contained in the function  $L_H$  by means of the Lamé (complex) parameter  $\mu$  and the (complex)  $S$ -wave velocity  $\beta$ , which is also in the matrix  $\mathbf{P}_L$ .

### A2 $P$ - $SV$ waves

In the same way as the previous case, by posing

$$\mathbf{r}^j(z) \equiv \begin{pmatrix} R_1^j(z; k) \\ R_2^j(z; k) \\ R_3^j(z; k) \\ R_4^j(z; k) \end{pmatrix} \quad (\text{A6})$$

ground-motion amplitudes at the surface can be written as (see Aki & Richards 1980)

$$\mathbf{r}^1(0) = \mathbf{P}_R(z^N, 0; k) \cdot \mathbf{V}_R(k) \cdot \begin{pmatrix} C_1 \\ C_2 \end{pmatrix}, \quad (\text{A7})$$

where  $\mathbf{P}_R(z_1, z_2; k)$  is the propagation matrix between the depths  $z_1$  and  $z_2$ ,  $C_1$  and  $C_2$  are the constants determined from initial conditions, and

$$\mathbf{V}_R(k) \equiv \begin{pmatrix} k & v \\ \gamma & k \\ -2\mu\gamma k & -\mu\chi \\ -\mu\chi & -2\mu vk \end{pmatrix}_{N+1},$$

where

$$\gamma^{N+1} \equiv \left[ k^2 - \left( \frac{\omega}{\alpha^{N+1}} \right)^2 \right]^{\frac{1}{2}},$$

$$v^{N+1} \equiv \left[ k^2 - \left( \frac{\omega}{\beta^{N+1}} \right)^2 \right]^{\frac{1}{2}},$$

$$\chi^{N+1} \equiv 2k^2 - \left( \frac{\omega}{\beta^{N+1}} \right)^2.$$

By following equations (A24, A25) and (A28) from Hisada (1994), the surface point load (A2) can be represented in terms of a stress discontinuity in the form

$$R_3^1(0; k) \equiv \begin{cases} R_H^*(k) \cdot \Psi_x, & \text{if } \mathbf{q} = \hat{\mathbf{x}} \\ R_H^*(k) \cdot \Psi_y, & \text{if } \mathbf{q} = \hat{\mathbf{y}} \end{cases}$$

$$R_4^1(0; k) \equiv R_V^*(k) \cdot \Psi_z,$$

with  $R_H^*(k) \equiv -\frac{k}{2\pi}$  and  $R_V^*(k) \equiv \frac{k}{2\pi}$ . Thus, given that

$$\mathbf{P}_R(z^N, 0; k) \equiv \begin{pmatrix} P_{11} & P_{12} & P_{13} & P_{14} \\ P_{21} & P_{22} & P_{23} & P_{24} \\ P_{31} & P_{32} & P_{33} & P_{34} \\ P_{41} & P_{42} & P_{43} & P_{44} \end{pmatrix}$$

$$\mathbf{S}_R(k) \equiv \begin{pmatrix} S_{11} & S_{12} \\ S_{21} & S_{22} \\ S_{31} & S_{32} \\ S_{41} & S_{42} \end{pmatrix} \equiv \mathbf{P}_R(z^N, 0; k) \cdot \mathbf{V}_R(k),$$

one has

$$\begin{pmatrix} R_3^1(0; k) \\ R_4^1(0; k) \end{pmatrix} = \begin{pmatrix} 0 & 0 & 1 & 0 \\ 0 & 0 & 0 & 1 \end{pmatrix} \cdot \mathbf{S}_R(k) \cdot \begin{pmatrix} C_1 \\ C_2 \end{pmatrix}.$$

Remembering that the Rayleigh waves characteristic function is the determinant of the submatrix  $\mathbf{S}_R(k)$  constituted by the last two lines

$$F_R(k) \equiv S_{31}S_{42} - S_{41}S_{32},$$

it follows that when  $F_R(k) \neq 0$ , one has

$$\begin{pmatrix} S_{31} & S_{32} \\ S_{41} & S_{42} \end{pmatrix}^{-1} = \frac{1}{F_R(k)} \begin{pmatrix} S_{42} & -S_{32} \\ -S_{41} & S_{31} \end{pmatrix}.$$

Since the zeroes of the Rayleigh waves characteristic equation are, at a fixed frequency, in a finite set, one can write for almost each  $k$

$$\begin{pmatrix} C_1 \\ C_2 \end{pmatrix} = \frac{1}{F_R(k)} \begin{pmatrix} S_{42} & -S_{32} \\ -S_{41} & S_{31} \end{pmatrix} \begin{pmatrix} R_3^1(0; k) \\ R_4^1(0; k) \end{pmatrix}.$$

Thus, from (A7) one has

$$\begin{aligned} \begin{pmatrix} R_1^1(0; k) \\ R_2^1(0; k) \end{pmatrix} &= \begin{pmatrix} S_{11} & S_{12} \\ S_{21} & S_{22} \end{pmatrix} \frac{1}{F_R(k)} \begin{pmatrix} S_{42} & -S_{32} \\ -S_{41} & S_{31} \end{pmatrix} \\ &\cdot \begin{pmatrix} R_3^1(0; k) \\ R_4^1(0; k) \end{pmatrix} = \frac{1}{F_R(k)} \\ &\cdot \begin{pmatrix} S_{11}S_{42} - S_{12}S_{41} & -S_{11}S_{32} + S_{12}S_{31} \\ S_{21}S_{42} - S_{22}S_{41} & -S_{21}S_{32} + S_{22}S_{31} \end{pmatrix} \begin{pmatrix} R_3^1(0; k) \\ R_4^1(0; k) \end{pmatrix} \\ &= \frac{1}{F_R(k)} \\ &\cdot \begin{pmatrix} (S_{11}S_{42} - S_{12}S_{41})R_3^1(0; k) & (S_{12}S_{31} - S_{11}S_{32})R_4^1(0; k) \\ (S_{21}S_{42} - S_{22}S_{41})R_3^1(0; k) & (S_{22}S_{31} - S_{21}S_{32})R_4^1(0; k) \end{pmatrix} \end{aligned}$$

for almost each  $k$ . Again, the ground-motion amplitude at the surface is linearly proportional to the applied surface load

$$\begin{pmatrix} R_{1,x} \\ R_{2,x} \end{pmatrix} = \frac{1}{F_R(k)} \begin{pmatrix} S_{11}S_{42} - S_{12}S_{41} \\ S_{21}S_{42} - S_{22}S_{41} \end{pmatrix} R_H^*(k) \Psi_x,$$

$$\begin{pmatrix} R_{1,y} \\ R_{2,y} \end{pmatrix} = \frac{1}{F_R(k)} \begin{pmatrix} S_{11}S_{42} - S_{12}S_{41} \\ S_{21}S_{42} - S_{22}S_{41} \end{pmatrix} R_H^*(k) \Psi_y,$$

$$\begin{pmatrix} R_{1,z} \\ R_{2,z} \end{pmatrix} = \frac{1}{F_R(k)} \begin{pmatrix} S_{12}S_{31} - S_{11}S_{32} \\ S_{22}S_{31} - S_{21}S_{32} \end{pmatrix} R_V^*(k) \Psi_z,$$

for almost each  $k$ . Given that

$$\begin{pmatrix} R_{1,H}(k) \\ R_{2,H}(k) \end{pmatrix} \equiv \frac{R_H^*(k)}{F_R(k)} \begin{pmatrix} S_{11}S_{42} - S_{12}S_{41} \\ S_{21}S_{42} - S_{22}S_{41} \end{pmatrix}, \quad k - \text{a.e.},$$

$$\begin{pmatrix} R_{1,V}(k) \\ R_{2,V}(k) \end{pmatrix} = \frac{R_V^*(k)}{F_R(k)} \begin{pmatrix} S_{12}S_{31} - S_{11}S_{32} \\ S_{22}S_{31} - S_{21}S_{32} \end{pmatrix}, \quad k - \text{a.e.}$$

such linear relationships have the simple form

$$\begin{pmatrix} R_{1,x} \\ R_{2,x} \end{pmatrix} = \begin{pmatrix} R_{1,H}(k) \\ R_{2,H}(k) \end{pmatrix} \Psi_x, \quad k - \text{a.e.},$$

$$\begin{pmatrix} R_{1,y} \\ R_{2,y} \end{pmatrix} = \begin{pmatrix} R_{1,H}(k) \\ R_{2,H}(k) \end{pmatrix} \Psi_y, \quad k - \text{a.e.},$$

$$\begin{pmatrix} R_{1,z} \\ R_{2,z} \end{pmatrix} = \begin{pmatrix} R_{1,V}(k) \\ R_{2,V}(k) \end{pmatrix} \Psi_z, \quad k - \text{a.e.}$$

Again, the viscosity is taken into account in the functions  $R_{j,H}$  and  $R_{j,V}$  ( $j = 1, 2$ ) by means of the Lamé (complex) parameters  $\lambda$ ,  $\mu$  and the (complex) body wave velocities  $\alpha$ ,  $\beta$ , also in the matrix  $\mathbf{P}_R$ .

## APPENDIX B

Components of the ground motion can be also expressed in terms of local Cartesian components

$$\begin{cases} u_x(r, \vartheta) \equiv u_r(r, \vartheta) \cos \vartheta - u_\vartheta(r, \vartheta) \sin \vartheta \\ u_y(r, \vartheta) \equiv u_r(r, \vartheta) \sin \vartheta + u_\vartheta(r, \vartheta) \cos \vartheta \\ u_z(r, \vartheta) \equiv u_z(r, \vartheta) \end{cases} \quad (\text{B1})$$

that is,

$$\begin{aligned} u_x(r, \vartheta) &= \Phi_x \{ \tilde{u}_r(r) \cos^2 \vartheta - \tilde{u}_\vartheta(r) \sin^2 \vartheta \} \\ &\quad + \Phi_y \{ \tilde{u}_r(r) + \tilde{u}_\vartheta(r) \} \cos \vartheta \sin \vartheta + \Phi_z u_r^*(r) \cos \vartheta, \\ u_y(r, \vartheta) &= \Phi_x \{ \tilde{u}_r(r) + \tilde{u}_\vartheta(r) \} \cos \vartheta \sin \vartheta \\ &\quad + \Phi_y \{ \tilde{u}_r(r) \sin^2 \vartheta - \tilde{u}_\vartheta(r) \cos^2 \vartheta \} + \Phi_z u_r^*(r) \sin \vartheta. \end{aligned}$$

The averages of these quantities vanish while the variance relative to the first component is

$$\mathcal{V}[u_x(r, \vartheta)] = \mathcal{M}[u_x(r, \vartheta) \cdot \overline{u_x(r, \vartheta)}] = \mathcal{V}_x(r, \vartheta) + \mathcal{K}_x(r, \vartheta),$$

where the variance and covariance terms are

$$\begin{aligned} \mathcal{V}_x(r, \vartheta) &= \mathcal{V}[\Phi_x] \cdot |\tilde{u}_r(r) \cdot \cos^2 \vartheta - \tilde{u}_\vartheta(r) \cdot \sin^2 \vartheta|^2 \\ &\quad + \mathcal{V}[\Phi_y] \cdot |\tilde{u}_r(r) + \tilde{u}_\vartheta(r)|^2 \cdot \cos^2 \vartheta \sin^2 \vartheta \\ &\quad + \mathcal{V}[\Phi_z] |u_r^*(r)|^2 \cdot \cos^2 \vartheta, \\ \mathcal{K}_x(r, \vartheta) &= 2 \cos \vartheta \sin \vartheta \mathcal{M}[\Phi_x \Phi_y] \\ &\quad \cdot \Re \left\{ [\tilde{u}_r(r) \cos^2 \vartheta - \tilde{u}_\vartheta(r) \sin^2 \vartheta] \cdot [\overline{\tilde{u}_r(r) + \tilde{u}_\vartheta(r)}] \right\} \\ &\quad + 2 \cos \vartheta \mathcal{M}[\Phi_x \Phi_z] \\ &\quad \cdot \Re \left\{ [\tilde{u}_r(r) \cos^2 \vartheta - \tilde{u}_\vartheta(r) \sin^2 \vartheta] \cdot \overline{u_r^*(r)} \right\} \\ &\quad + 2 \cos \vartheta \mathcal{M}[\Phi_y \Phi_z] \Re \left\{ [\tilde{u}_r(r) + \tilde{u}_\vartheta(r)] \cdot \overline{u_r^*(r)} \right\}, \end{aligned}$$

respectively. In the same way,

$$\begin{aligned} \mathcal{V}[u_y(r, \vartheta)] &= \mathcal{M}[u_y(r, \vartheta) \cdot \overline{u_y(r, \vartheta)}] = \mathcal{V}_y(r, \vartheta) + \mathcal{K}_y(r, \vartheta), \\ \mathcal{V}_y(r, \vartheta) &= \mathcal{V}[\Phi_x] |\tilde{u}_r(r) + \tilde{u}_\vartheta(r)|^2 \cos^2 \vartheta \sin^2 \vartheta \\ &\quad + \mathcal{V}[\Phi_y] |\tilde{u}_r(r) \sin^2 \vartheta - \tilde{u}_\vartheta(r) \cos^2 \vartheta|^2 \\ &\quad + \mathcal{V}[\Phi_z] |u_r^*(r)|^2 \sin^2 \vartheta \\ \mathcal{K}_y(r, \vartheta) &= 2 \cos \vartheta \sin \vartheta \mathcal{M}[\Phi_x \Phi_y] \\ &\quad \cdot \Re \left\{ [\tilde{u}_r(r) \sin^2 \vartheta - \tilde{u}_\vartheta(r) \cos^2 \vartheta] \cdot [\overline{\tilde{u}_r(r) + \tilde{u}_\vartheta(r)}] \right\} \\ &\quad + 2 \sin \vartheta \mathcal{M}[\Phi_x \Phi_z] \Re \left\{ [\tilde{u}_r(r) + \tilde{u}_\vartheta(r)] \cdot \overline{u_r^*(r)} \right\} \\ &\quad + 2 \sin \vartheta \mathcal{M}[\Phi_y \Phi_z] \\ &\quad \cdot \Re \left\{ [\tilde{u}_r(r) \sin^2 \vartheta - \tilde{u}_\vartheta(r) \cos^2 \vartheta] \cdot \overline{u_r^*(r)} \right\}. \end{aligned}$$



By using the relationships in Appendix A, one can obtain total variances relative to the distributed sources given in Section 2; the angular integrals relative to the covariance term  $\mathcal{K}_x$  are

$$\begin{aligned}
& \int_0^{2\pi} \Re \left\{ \left[ \tilde{u}_r(r) \cos^2 \vartheta - \tilde{u}_\vartheta(r) \sin^2 \vartheta \right] \cdot \overline{[\tilde{u}_r(r) + \tilde{u}_\vartheta(r)]} \right\} \\
& \quad \cdot \cos \vartheta \sin \vartheta \, d\vartheta \\
&= \Re \left\{ \tilde{u}_r(r) \cdot \overline{[\tilde{u}_r(r) + \tilde{u}_\vartheta(r)]} \right\} \cdot \int_0^{2\pi} \cos^3 \vartheta \sin \vartheta \, d\vartheta \\
& \quad - \Re \left\{ \tilde{u}_\vartheta(r) \cdot \overline{[\tilde{u}_r(r) + \tilde{u}_\vartheta(r)]} \right\} \cdot \int_0^{2\pi} \cos \vartheta \sin^3 \vartheta \, d\vartheta = 0, \\
& \int_0^{2\pi} \Re \left\{ \left[ \tilde{u}_r(r) \cos^2 \vartheta - \tilde{u}_\vartheta(r) \sin^2 \vartheta \right] \cdot \overline{u_r^*(r)} \right\} \cos \vartheta \, d\vartheta \\
&= \int_0^{2\pi} \Re \left\{ \tilde{u}_r(r) \cdot \overline{u_r^*(r)} \right\} \cos^3 \vartheta \, d\vartheta \\
& \quad - \int_0^{2\pi} \Re \left\{ \tilde{u}_\vartheta(r) \cdot \overline{u_r^*(r)} \right\} \cos \vartheta \sin^2 \vartheta \, d\vartheta = 0, \\
& \int_0^{2\pi} \Re \left\{ [\tilde{u}_r(r) + \tilde{u}_\vartheta(r)] \cdot \overline{u_r^*(r)} \right\} \cos \vartheta \, d\vartheta \\
&= \Re \left\{ [\tilde{u}_r(r) + \tilde{u}_\vartheta(r)] \cdot \overline{u_r^*(r)} \right\} \cdot \int_0^{2\pi} \cos \vartheta \, d\vartheta = 0.
\end{aligned}$$

Thus, for all  $r_1$  and  $r_2$ ,

$$\begin{aligned}
& \int_{r_1}^{r_2} \int_0^{2\pi} \mathcal{K}_x(r, \vartheta) r \, d\vartheta \, dr \\
&= \int_{r_1}^{r_2} \int_0^{2\pi} \mathcal{K}_y(r, \vartheta) r \, d\vartheta \, dr = 0,
\end{aligned} \tag{B2}$$

and the only terms that contribute to the total variances are

$$\begin{aligned}
& \int_0^{2\pi} \mathcal{V}_x(r, \vartheta) \, d\vartheta = \sigma^2 \sigma_x^2 \\
& \quad \cdot \int_0^{2\pi} \left\{ \left\{ \Re [\tilde{u}_r(r) \cos^2 \vartheta - \tilde{u}_\vartheta(r) \sin^2 \vartheta] \right\}^2 \right. \\
& \quad \left. + \left\{ \Im [\tilde{u}_r(r) \cos^2 \vartheta - \tilde{u}_\vartheta(r) \sin^2 \vartheta] \right\}^2 \right\} d\vartheta \\
& \quad + \sigma^2 \sigma_y^2 |\tilde{u}_r(r) + \tilde{u}_\vartheta(r)|^2 \int_0^{2\pi} \cos^2 \vartheta \sin^2 \vartheta \, d\vartheta \\
& \quad + \sigma^2 \sigma_z^2 |u_r^*(r)|^2 \int_0^{2\pi} \cos^2 \vartheta \, d\vartheta \\
&= \sigma^2 \sigma_x^2 \int_0^{2\pi} \left\{ \left\{ \Re [\tilde{u}_r(r)] \cos^2 \vartheta - \Re [\tilde{u}_\vartheta(r)] \sin^2 \vartheta \right\}^2 \right. \\
& \quad \left. + \left\{ \Im [\tilde{u}_r(r)] \cos^2 \vartheta - \Im [\tilde{u}_\vartheta(r)] \sin^2 \vartheta \right\}^2 \right\} d\vartheta + \\
& \quad + \frac{\pi}{4} \sigma^2 \sigma_y^2 |\tilde{u}_r(r) + \tilde{u}_\vartheta(r)|^2 + \pi \sigma^2 \sigma_z^2 |u_r^*(r)|^2
\end{aligned}$$

$$\begin{aligned}
&= \sigma^2 \sigma_x^2 \left\{ \left\{ \Re [\tilde{u}_r(r)]^2 + \Im [\tilde{u}_r(r)]^2 \right\} \int_0^{2\pi} \cos^4 \vartheta \, d\vartheta \right. \\
& \quad + \left\{ \Re [\tilde{u}_\vartheta(r)]^2 + \Im [\tilde{u}_\vartheta(r)]^2 \right\} \int_0^{2\pi} \sin^4 \vartheta \, d\vartheta \\
& \quad - 2 \left\{ \Re [\tilde{u}_r(r)] \Re [\tilde{u}_\vartheta(r)] + \Im [\tilde{u}_r(r)] \Im [\tilde{u}_\vartheta(r)] \right\} \\
& \quad \cdot \int_0^{2\pi} \cos^2 \vartheta \sin^2 \vartheta \, d\vartheta \left. \right\} \\
& \quad + \frac{\pi}{4} \sigma^2 \sigma_y^2 |\tilde{u}_r(r) + \tilde{u}_\vartheta(r)|^2 + \pi \sigma^2 \sigma_z^2 |u_r^*(r)|^2 \\
&= \pi \sigma^2 \left\{ \frac{3}{4} \sigma_x^2 [|\tilde{u}_r(r)|^2 + |\tilde{u}_\vartheta(r)|^2] \right. \\
& \quad - \frac{1}{2} \sigma_x^2 \{ \Re [\tilde{u}_r(r)] \Re [\tilde{u}_\vartheta(r)] + \Im [\tilde{u}_r(r)] \Im [\tilde{u}_\vartheta(r)] \} \\
& \quad \left. + \frac{1}{4} \sigma_y^2 |\tilde{u}_r(r) + \tilde{u}_\vartheta(r)|^2 + \sigma_z^2 |u_r^*(r)|^2 \right\},
\end{aligned}$$

and

$$\begin{aligned}
& \int_0^{2\pi} \mathcal{V}_y(r, \vartheta) \, d\vartheta = \pi \sigma^2 \left\{ \frac{1}{4} \sigma_x^2 |\tilde{u}_r(r) + \tilde{u}_\vartheta(r)|^2 \right. \\
& \quad + \frac{3}{4} \sigma_y^2 [|\tilde{u}_r(r)|^2 + |\tilde{u}_\vartheta(r)|^2] - \frac{1}{2} \sigma_y^2 \{ \Re [\tilde{u}_r(r)] \Re [\tilde{u}_\vartheta(r)] \\
& \quad \left. + \Im [\tilde{u}_r(r)] \Im [\tilde{u}_\vartheta(r)] \} + \sigma_z^2 |u_r^*(r)|^2 \right\}.
\end{aligned}$$

In the end, one has

$$\begin{aligned}
\mathcal{V}_x^{\text{TOT}} &= \int_{r_1}^{r_2} \int_0^{2\pi} \mathcal{V}_x(r, \vartheta) r \, d\vartheta \, dr \\
&= \pi \sigma^2 \left\{ \frac{3}{4} \sigma_x^2 \int_{r_1}^{r_2} [|\tilde{u}_r(r)|^2 + |\tilde{u}_\vartheta(r)|^2] r \, dr - \frac{1}{2} \sigma_x^2 \right. \\
& \quad \cdot \int_{r_1}^{r_2} \{ \Re [\tilde{u}_r(r)] \Re [\tilde{u}_\vartheta(r)] + \Im [\tilde{u}_r(r)] \Im [\tilde{u}_\vartheta(r)] \} r \, dr \\
& \quad + \frac{1}{4} \sigma_y^2 \int_{r_1}^{r_2} |\tilde{u}_r(r) + \tilde{u}_\vartheta(r)|^2 r \, dr \\
& \quad \left. + \sigma_z^2 \int_{r_1}^{r_2} |u_r^*(r)|^2 r \, dr \right\}
\end{aligned}$$

and

$$\begin{aligned}
\mathcal{V}_y^{\text{TOT}} &= \int_{r_1}^{r_2} \int_0^{2\pi} \mathcal{V}_y(r, \vartheta) r \, d\vartheta \, dr \\
&= \pi \sigma^2 \left\{ \frac{1}{4} \sigma_x^2 \int_{r_1}^{r_2} |\tilde{u}_r(r) + \tilde{u}_\vartheta(r)|^2 r \, dr \right. \\
& \quad + \frac{3}{4} \sigma_y^2 \int_{r_1}^{r_2} [|\tilde{u}_r(r)|^2 + |\tilde{u}_\vartheta(r)|^2] r \, dr - \frac{1}{2} \sigma_y^2 \\
& \quad \cdot \int_{r_1}^{r_2} \{ \Re [\tilde{u}_r(r)] \Re [\tilde{u}_\vartheta(r)] + \Im [\tilde{u}_r(r)] \Im [\tilde{u}_\vartheta(r)] \} r \, dr \\
& \quad \left. + \sigma_z^2 \int_{r_1}^{r_2} |u_r^*(r)|^2 r \, dr \right\}.
\end{aligned}$$

As regards the  $z$  component, one also has (45).